Title:

Inhibitory basal ganglia nuclei differentially innervate pedunculopontine nucleus subpopulations and evoke opposite motor and valence behaviors.

Author list and affiliations:

[1,2,3]Michel Fallah
[2]Kenea C Udobi
[2]Aleksandra E Swiatek
[2]Chelsea B Scott
[2,4]Rebekah C Evans*

[1]Interdisciplinary Program in Neuroscience, Georgetown University, Washington, DC, USA 20007
[2]Department of Neuroscience, Georgetown University Medical Center, Washington, DC, USA 20007
[3]Senior author
[4]Lead contact

Lead Contact footnote:

*Rebekah Evans, Ph.D.
re285@georgetown.edu
Department of Neuroscience
Georgetown University
3970 Reservoir Rd. NW, NRB EG31
Washington DC

Email addresses:

re285@georgetown.edu

Graphical Abstract:

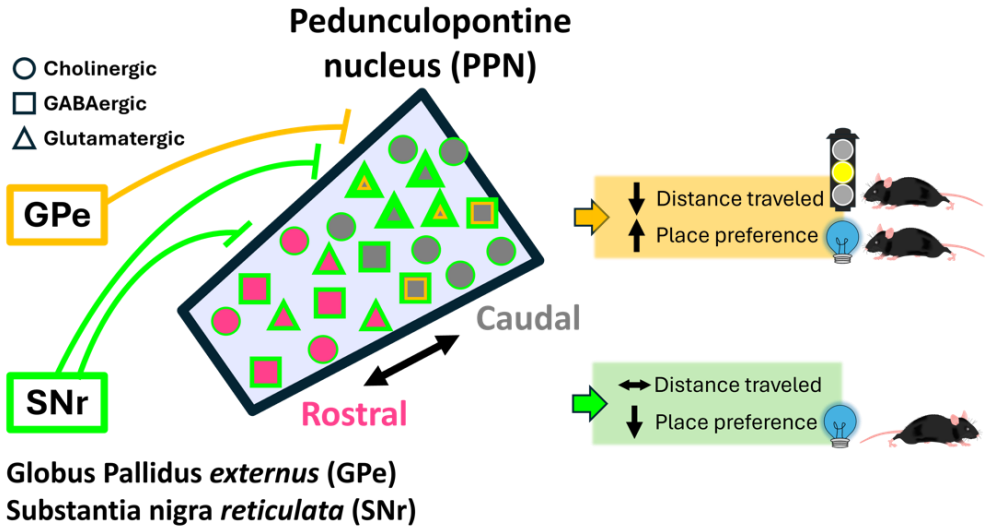

Summary:
The canonical basal ganglia model predicts that the substantia nigra *pars reticulata* (SNr) and the globus pallidus *externa* (GPe) will have specific effects on locomotion: the SNr inhibiting locomotion and the GPe enhancing it. In this manuscript, we use *in vivo* optogenetics to show that a projection-defined neural subpopulation within each structure exerts non-canonical effects on locomotion. These non-canonical subpopulations are defined by their projection to the pedunculopontine nucleus (PPN) and mediate opposing effects on reward. To understand how these structures differentially modulate the PPN, we use *ex vivo* whole-cell recording with optogenetics to comprehensively dissect the SNr and GPe connections to regionally- and molecularly-defined populations of PPN neurons. The SNr inhibits all PPN subtypes, but most strongly inhibits caudal glutamatergic neurons. The GPe selectively inhibits caudal glutamatergic and GABAergic neurons, avoiding both cholinergic and rostral cells. This circuit characterization reveals non-canonical basal ganglia pathways for locomotion and valence.

Key words: basal ganglia; brainstem; locomotion; reward; mesencephalic locomotor region; inhibition; electrophysiology; optogenetics; substantia nigra; pedunculopontine nucleus

Introduction:

The pedunculopontine nucleus (PPN) is a brainstem structure heavily interconnected with subcortical structures, such as the basal ganglia, thalamus, and spinal cord. The PPN has been implicated in locomotor control and valence processing[1–4]. However, understanding PPN circuitry is complicated by its anatomical and molecular heterogeneity. It has three molecularly-defined cell types, distinguished by their major neurotransmitter[5] and distinct rostral and caudal topography. While cholinergic and glutamatergic neurons are more densely packed in the caudal PPN, GABAergic neurons are more densely packed in the rostral PPN[5,6]. These molecularly-defined populations display very minimal overlap[5,7,8]. This unique topography has been conserved across species[9–11], but it is unknown how the basal ganglia connects to each of the distinct cell types in the rostral and caudal PPN regions to modulate locomotor and valence outputs.

While the PPN interacts with all basal ganglia nuclei[3,9], the inhibitory inputs from the substantia nigra *pars reticulata* (SNr) and the globus pallidus *externus* (GPe) to the PPN are of particular interest because of their roles in the canonical motor pathways for ‘stop’ and ‘go,’ respectively. Both the SNr and GPe are known to send axonal projections to the PPN[12–18]. Previous studies have identified SNr and GPe monosynaptic connections to the PPN cholinergic and glutamatergic neurons using rabies tracing[13–17]. However, inputs to the GABAergic neurons have only been described in terms of the entire mesencephalic locomotor region (MLR), which extends beyond the PPN[14]. While SNr projections to MLR GABAergic neurons were identified but cannot be isolated to the PPN, GPe projections to the GABAergic MLR neurons were not detected[14]. Of note, these previous studies consider the PPN as a whole rather than separating its rostral and caudal subregions. While viral tracing can provide insight into neuroanatomical connections, limitations of these techniques[19–21] and evidence that the rostral and

caudal PPN may have distinct functions[22–24] prompt a need for electrophysiological studies to determine whether the SNr and GPe inputs differentially innervate regionally-defined PPN neurons.

Optogenetic manipulations of the molecularly-defined PPN cell types have resulted in variable, and sometimes contradictory, locomotor and valence behaviors[7,14,16,17,22–32]. More recent studies have refined our understanding of these opposing behavioral effects by selectively stimulating the rostral or caudal GABAergic and glutamatergic PPN neurons[22–24]. In the basal ganglia, direct stimulation of molecularly-defined SNr and GPe subpopulations can also have distinct effects on locomotion and valence[33–41]. Despite the potential for the basal ganglia to modify behavior through the motor brainstem[14], it is not clear how the SNr and GPe influence the rostral and caudal PPN to modify locomotion and valence.

Here, we use whole-cell patch clamp electrophysiology paired with optogenetics to selectively stimulate the SNr or GPe axons while recording inhibitory inputs to the cholinergic, GABAergic, and glutamatergic PPN neurons to comprehensively characterize the strength and pattern of inhibition across the rostrocaudal PPN axis. We find that the GPe preferentially inhibits caudal GABAergic and glutamatergic PPN neurons whereas the SNr most strongly inhibits a caudal 'hotspot' of PPN glutamatergic neurons. Stimulating SNr or GPe axons over the PPN *in vivo* evokes opposing valence processing outcomes with place aversion during SNr stimulation and place preference during GPe stimulation. Surprisingly, and counter to the predictions of the canonical basal ganglia model, we find that stimulating PPN-projecting SNr neurons increases locomotion, while the GPe decreases locomotion through its projections to the PPN. While both the SNr and GPe inhibit the PPN, our results show that each nucleus differentially modulates the activity of specific cell types in the rostral and caudal PPN and are implicated in non-canonical basal ganglia circuits for modulating locomotion and valence processing.

Results:

SNr and GPe axons display distinct distribution patterns across the rostral and caudal PPN.

To characterize the axon distribution pattern from the SNr and GPe throughout the rostral and caudal extent of the PPN, we stereotaxically injected a channelrhodopsin virus with a fluorescent marker (AAV1-hSyn-ChR2-eYFP) into either the SNr or GPe of ChAT-Cre/Ai9-tdTomato mice (**Figure 1A&C**). We sliced 200 μm sagittal slices from mouse brains three weeks after viral injection and cleared the brain slices using the CUBIC clearing method[42]. Using the red fluorescent ChAT-positive neurons to define the borders of the PPN, we found that SNr axons appear in both the rostral and caudal PPN. The SNr axons fill the rostral PPN evenly, but appear more distinctly clustered in specific areas of the caudal PPN (**Figure 1B**), whereas GPe axonal projections more densely fill the caudal region and strikingly avoid the rostral region (**Figure 1D**). These anatomical findings predict that the SNr will inhibit both rostral and caudal PPN neurons, while the GPe will selectively inhibit the caudal PPN. However, this axon imaging method does not reveal whether these axons form functional synapses with the neurons in the PPN and does not provide information on the strength of inhibition from each structure onto specific PPN cell types. Therefore, to evaluate the functional connectivity

and synaptic characteristics from these inhibitory basal ganglia output structures to regionally- and molecularly-defined PPN neural subpopulations, we systematically recorded the inhibitory input to the rostral and caudal PPN from the SNr and GPe in three genetic mouse lines (ChAT-cre, Vgat-cre, and Vglut2-cre) to identify the cholinergic, GABAergic, and glutamatergic PPN subpopulations, respectively (see Figure S1).

The SNr inhibits cholinergic neurons in both the rostral and caudal PPN to a similar extent, but evokes stronger rebound in rostral neurons.

To evaluate the functional connection between the SNr and cholinergic PPN neurons, we performed *ex vivo* whole-cell patch clamp electrophysiology paired with optogenetics to record synaptic currents in ChAT-Cre/Ai9-tdTomato mice injected with ChR2 in the SNr three weeks prior (**Figure 2A**). Neurons were targeted for whole-cell patch clamp in both the rostral and caudal PPN across three sagittal slices to evaluate the medial to lateral extent of the PPN (**Figure 2B**). To measure optically-evoked inhibitory post-synaptic currents (oIPSCs), cholinergic PPN neurons were held at -50 mV in whole-cell voltage clamp and blue (470 nm) light was applied (2 ms pulse duration, 13 mW) to activate the ChR2-infected SNr axons. In connected neurons, inhibitory currents were recorded in the presence of glutamatergic receptor blockers (AP5, NBQX, CNQX) during stimulation (**Figure 2C**). In a subset of neurons, a GABA-a receptor blocker, GABAzine, was applied to confirm the oIPSCs were GABA-mediated (**Figure 2C**). GABAzine eliminated SNr-evoked inhibitory currents in most cells, but a small residual current remained in some cells (see *Methods* for details). We found that all rostral (n=19/19 cells, N=6 mice) and essentially all caudal (n=26/27, N=6) recorded cholinergic PPN neurons responded to SNr axon activation with an observable oIPSC (**Figure 2D**).

To determine whether the SNr input to the rostral and caudal PPN cholinergic neurons differed in synaptic strength, we measured the amplitude of each oIPSC in a 20 Hz train of 2 ms optical stimulations applied for 2 seconds. We found that the oIPSCs ranged from tens to hundreds of picoamperes (pA) in both groups and there was no significant difference between the average amplitude of the first oIPSC in the stimulus train onto rostral vs caudal cholinergic neurons (mean ± SEM; first oIPSC n=15 Rostral: 92.6 ± 18 pA, n=20 Caudal: 115.2 ± 17 pA; unpaired t-test, t=0.9041, p=0.3725; **Figure 2E&F**). Going forward, the first oIPSC amplitude of the train will be referred to as the first oIPSC.

While the rostral and caudal anatomical separation of PPN neurons is commonly used, it remains a relatively coarse division. Therefore, we carefully mapped the location of each recorded cholinergic PPN neuron by matching slices to their bregma reference in the Paxinos and Franklin's mouse brain atlas and aligning the midline of cholinergic neuron distribution which separates the loosely spread rostral neurons and densely packed caudal neurons (See *Methods* for details, **Figure 2G**). The strength of the SNr inhibitory connection is depicted by a color scale representative of the first oIPSC (**Figure 2G, *right***). Throughout both the rostral and caudal PPN, neurons receiving larger inputs from the SNr are intermixed with neurons receiving smaller inputs.

The postsynaptic response to a 2-second 20 Hz stimulation train can undergo short-term synaptic plasticity which either depresses or facilitates current amplitude with subsequent stimulations. To compare short-term synaptic plasticity characteristics between rostral and caudal cholinergic PPN neurons, we normalized the amplitude of each current in the train to the first current. We found that the oIPSC amplitude remained relatively constant with each subsequent pulse in both rostral and caudal cholinergic neurons (**Figure 2H**). In addition, the paired-pulse ratio (PPR) of the peak of the first two currents in the stimulation train did not differ (mean ± SEM; PPR n=15 Rostral: 0.96 ± 0.04, n=20 Caudal: 0.97 ± 0.05; unpaired t-test, t=0.1082, p=0.9145; **Figure 2I**). While the postsynaptic currents in some cells displayed short-term synaptic plasticity, these data show that SNr synaptic inputs onto cholinergic neurons do not undergo significant short-term synaptic plasticity in either the rostral or caudal PPN.

Although oIPSC amplitude is indicative of the strength of a synapse, it does not always correlate with the functional impact on a neuron's action potential output[20,43,44]. Because cholinergic PPN neurons display spontaneous firing[45–49], we characterized the impact of SNr-mediated inhibition on action potential firing rate. While optically stimulating SNr axons with the same 20 Hz blue light protocol as above, we observed a decrease in firing rate in the recorded cholinergic PPN neuron (**Figure 2J**). Both rostral and caudal neuronal populations showed significant inhibition compared to their pre-optical stimulation firing (2way ANOVA, p=0.0154; Tukey test, %Frequency Pre vs During Stimulation Rostral p<0.0001, Pre vs During Caudal p<0.0001), and there was no significant difference between the percent frequency change in rostral and caudal neurons during SNr axon stimulation (mean ± SEM; %Frequency During Stimulation n=14 Rostral: 35.62 ± 8.87 %, n=23 Caudal: 52.11 ± 8.43 %; 2way ANOVA, p=0.0154; Tukey test, Rostral vs Caudal p=0.1133; **Figure 2K**). There was also no rostrocaudal difference in cholinergic neuron firing when measuring the absolute decrease in firing frequency during optical stimulation [median (IQR); ΔFrq During Opto n=14 Rostral: -2.47 Hz (-3.37 to -1.44 Hz), n=23 Caudal: -2.10 Hz (-3.11 to -0.84 Hz); Mann Whitney, U=131, p=0.3602; **Figure 2L**]. These data show that the SNr equally inhibits action potential firing in rostral and caudal PPN cholinergic neurons.

Post-inhibitory rebound firing has been observed in the PPN as well as other brainstem structures[48,50–55] and is associated with greater excitability, temporal encoding, and generation of oscillatory activity[56]. Indeed, we found that the rostral and caudal cholinergic PPN neurons exhibited an increase in action potential firing after inhibition (2way ANOVA, p=0.0154; Tukey test, %Frequency Pre vs. Post Stimulation Rostral p=0.0013, Pre vs Post Caudal p<0.0012; **Figure 2K**). This is in agreement with previous literature showing rebound spikes following inhibitory postsynaptic potentials recorded in PPN neurons of male rats during electrical stimulation of the SNr[50,51]. However, we found that the rostral cholinergic neurons experienced greater increases in post-inhibitory rebound excitation compared with caudal cholinergic neurons (mean ± SEM; %Frequency Post Stimulation n=14 Rostral: 136.1 ± 7.8 %, n=23 Caudal: 119.1 ± 4.6 %; 2way ANOVA, p=0.0154; Tukey test, Rostral vs Caudal p=0.0310; **Figure 2K**). Rostral neurons also show a significantly larger increase in rebound activity as measured by the absolute change in rebound frequency [median (IQR); ΔRebFrq n=14 Rostral: 1.64 Hz (1.00 to 2.17 Hz), n=22 Caudal: 0.83 Hz (0.42 to 1.14 Hz); Mann Whitney, U=79, p=0.0142; **Figure 2M**]. This aligns with previous findings showing that

rostral cholinergic neurons tend to have stronger intrinsic rebound activity compared to caudal neurons[48]. Importantly, we show that such rebound can be evoked by synaptic inhibition from the SNr.

To detect trends among SNr connectivity characteristics and intrinsic electrophysiological properties of cholinergic PPN neurons, we performed a correlation analysis to determine the strength and directionality of the relationship among five parameters [first oIPSC, PPR, ΔFrq During Opto, pre-optical stimulation frequency (Pre-Opto Frq), and ΔRebFrq] (**Figure 2N**). We found a weak but significant negative correlation between the frequency decrease during SNr axon stimulation and the rebound frequency increase (Spearman r=-0.372, p=0.039, **Figure 2N&O**). This finding is expected since strong inhibition is more effective at producing rebound activity than weak inhibition. However, rostral PPN cholinergic neurons do not receive significantly stronger inhibition from the SNr compared with caudal cholinergic neurons (**Figure 2F&L**). Therefore, larger rebound frequency in rostral neurons is likely due to differences in intrinsic cellular properties[48]. Put together, these findings show that the SNr inhibits rostral and caudal cholinergic PPN neurons to a similar extent, but evokes stronger rebound firing in the rostral neurons.

The SNr inhibits GABAergic neurons in both the rostral and caudal PPN to a similar extent.

While there are several rabies tracing studies suggesting SNr axons project to the cholinergic and glutamatergic PPN neurons[13–17], SNr projections to the GABAergic PPN neurons are inferred from a study of the entire mesencephalic locomotor region[14] and a characterization of their synaptic strength has not been conducted. Therefore, we evaluated the synaptic characteristics between the SNr and GABAergic neurons in the rostral and caudal PPN. In Vgat-Cre/Ai9-tdTomato mice, we injected ChR2 into the SNr to optically stimulate axons over the PPN while patching Vgat+ GABAergic PPN neurons (**Figure 3A**). We post-hoc stained the slices for ChAT+ neurons to verify the location of all patched GABAergic neurons within the cholinergic PPN. We found that all rostral (n=12/12, N=6) and most caudal (n=20/22, N=6) recorded GABAergic neurons received inhibitory input from the SNr (**Figure 3B**).

Although there was no major difference in the proportion of GABAergic neurons receiving inhibitory input from the SNr in the rostral vs caudal PPN, we compared the current amplitudes to characterize the synaptic strength of this connection. Both the oIPSC amplitudes across the 2 second stimulation and the first oIPSC showed no difference between rostral and caudal GABAergic neurons [median (IQR); first oIPSC n=9 Rostral: 76.5 pA (27.0 to 209.9 pA), n=13 Caudal: 59.7 pA (37.7 to 269.7 pA); Mann Whitney, U=50, p=0.6005; **Figure 3C&D**]. While the first oIPSC was not significantly different between rostral and caudal GABAergic neurons, the variability among caudal GABAergic neurons shows an interesting division between a subgroup responding with very small (<60 pA) amplitude currents and another subgroup responding with currents more than triple that amplitude, with one neuron responding with a 2.2 nA inhibitory current. We mapped the location of each recorded GABAergic neuron, as described above, and found no specific location corresponding with the neurons receiving stronger SNr inhibition across the PPN landscape (**Figure 3E**). These

findings suggest that GABAergic PPN neurons may be even further divided into distinct subpopulations defined by either strong or weak SNr input.

We also did not observe any differences in short-term synaptic plasticity between rostral and caudal GABAergic neurons (**Figure 3F**) and found no significant difference in PPR between rostral and caudal GABAergic neurons [median (IQR); PPR n=9 Rostral: 1.01 (0.88 to 1.16), n=13 Caudal: 1.06 (0.96 to 1.15); Mann Whitney, U=48, p=0.5123; **Figure 3G**]. This shows that, similar to the SNr connection with cholinergic PPN neurons, SNr input to the GABAergic PPN does not show significant short-term synaptic plasticity in either the rostral or caudal region.

Because GABAergic PPN neurons display spontaneous firing[49], we recorded action potential firing in current clamp while optically stimulating the SNr axons. The percent inhibition was not significantly different between rostral and caudal neurons (mean ± SEM; %Frequency During Stimulation n=7 Rostral: 37.91 ± 15.91 %, n=19 Caudal: 30.68 ± 8.03 %; 2way ANOVA, p=0.4662; **Figure 3H**), and there was no difference in rebound firing frequency (mean ± SEM; %Frequency Post Stimulation n= 7 Rostral: 100.0 ± 14.6 %, n=19 Caudal: 113.2 ± 5.2 %; 2way ANOVA, p=0.4662; **Figure 3H**). There was also no difference in the absolute frequency change during optical stimulation between rostral and caudal neurons [median (IQR); ΔFrq During Opto n=7 Rostral: -5.03 (-5.55 to -1.34) Hz, n=19 Caudal: -4.29 (-11.02 to -2.94) Hz; Mann Whitney, U=55, p=0.5336; **Figure 3I**]. These data show that the SNr equally inhibits action potential firing in rostral and caudal GABAergic PPN neurons and does not evoke significant rebound firing in this neural population.

While we found that the SNr inhibits the rostral and caudal GABAergic PPN neurons to a similar extent, there was greater variability in synaptic strength and impact on neuronal action potential firing among caudal GABAergic neurons. This strong variability suggests that GABAergic PPN neurons may be divided into functionally distinct neural types that do not correspond to their rostrocaudal anatomical location. To determine if the neurons receiving larger inhibitory currents have distinct characteristics, we performed a correlation analysis (**Figure 3J**). As expected, we found that the absolute frequency reduction during inhibition is correlated with the first oIPSC amplitude recorded in a cell (Spearman r=-0.755, p=0.001; **Figure 3K**). Surprisingly, however, we found a significant negative correlation between PPR and the pre-optical stimulation frequency (Pre-Opto Frq). Specifically, input to slower-firing neurons displayed greater short-term synaptic facilitation. This finding supports the idea that multiple functional neural subpopulations may be present within the GABAergic PPN population. Together, these results show that the SNr functionally inhibits GABAergic neurons across the rostrocaudal extent of the PPN, but suggests the presence of additional heterogeneity within the GABAergic PPN population.

The SNr differentially inhibits the rostral and caudal glutamatergic PPN neurons.

Previous rabies tracing anatomical studies have shown SNr inputs to glutamatergic PPN neurons[14,16,17], but a full characterization of their synaptic strength and rostral and caudal connectivity has not been conducted. In Vglut2-Cre/Ai9-tdTomato mice, we injected ChR2 into the SNr to optically stimulate axons over the PPN while patching Vglut2+ glutamatergic neurons in the PPN (**Figure 4A**). While holding cells at -50mV and applying 470 nm blue light stimulation, neurons were identified as connected if

oIPSCs were observed. Similar to our findings in cholinergic and GABAergic neurons, we found that all rostral (n=19/19, N=6) and all caudal (n=28/28, N=6) recorded glutamatergic neurons received inhibitory input from the SNr (**Figure 4B**).

Comparing the oIPSC amplitudes across the 20 Hz train, we discovered that the caudal glutamatergic neurons receive larger inhibitory currents than rostral glutamatergic neurons (**Figure 4C**). The median first oIPSC measured in caudal glutamatergic neurons was also significantly larger than those recorded in rostral neurons [median (IQR); first oIPSC n=13 Rostral: 61.6 pA (19.2 to 113.9 pA), n=13 Caudal: 313.5 pA (143.8 to 729.1 pA); Mann Whitney, U=29, p=0.0035; **Figure 4D**]. After post-hoc staining for the cholinergic PPN and mapping the location of each recorded glutamatergic PPN neuron as described above, we identified a 'hotspot' of strong SNr inhibition in a medial-caudal group of glutamatergic neurons (**Figure 4E**). This finding shows that a subset of caudal PPN neurons preferentially receive exceptionally strong SNr input.

To determine whether the SNr input to the rostral and caudal PPN show differential short-term synaptic plasticity, we compared the normalized oIPSC amplitudes. We found that inhibitory inputs to the rostral glutamatergic neurons display short-term synaptic facilitation with amplitudes increasing in subsequent stimulations (**Figure 4F**). However, strong facilitation occurred in only a few neurons that drove the mean upward (**Figure 4G**) and there was no significant difference between the PPR observed in rostral and caudal glutamatergic neurons when activating SNr axons [median (IQR); PPR n=13 Rostral: 1.07 (0.86 to 1.38), n=13 Caudal: 0.92 (0.89 to 1.02); Mann Whitney, U=77, p=0.7241; **Figure 4G**].

Because glutamatergic PPN neurons spontaneously fire[16,49], we wanted to determine if larger inhibitory currents mediated larger decreases in the firing rate of caudal PPN neurons. Therefore, we recorded tonic action potential firing in glutamatergic PPN neurons while optically stimulating SNr axons (**Figure 4H**). Although inhibition measured as the percent of pre-optical stimulation firing frequency was not significantly different between rostral and caudal neurons (mean ± SEM; %Frequency During Stimulation n=13 Rostral: 32.62 ± 10.21 %, n=17 Caudal: 24.71 ± 7.30 %; 2way ANOVA, p=0.7320; **Figure 4I**), we found that the absolute frequency decrease was significantly larger in caudal glutamatergic neurons compared to rostral neurons during SNr stimulation [median (IQR); ΔFrq During Opto n=13 Rostral: -3.21 Hz (-12.21 to -1.95 Hz), n=17 Caudal: -14.08 Hz (-20.04 to -6.07 Hz); Mann Whitney, U=55, p=0.0197; **Figure 4J**]. To examine the discrepancy between the percent decrease and the absolute decrease in firing frequency, we compared the spontaneous firing frequency between rostral and caudal glutamatergic neurons in cells that had no holding current applied. We found that caudal glutamatergic neurons fire faster than rostral glutamatergic neurons [median (IQR); Spontaneous Frequency n=11 Rostral: 6.8 Hz (5.4 to 17.2 Hz), n=16 Caudal: 20.6 Hz (11.2 to 37.2 Hz); Mann Whitney, U=45, p=0.0343; **Figure 4K]**. Together, these findings show that fast-firing caudal glutamatergic PPN neurons receive larger SNr-mediated IPSCs and display greater decreases in their action potential firing.

Since we found that the caudal glutamatergic neurons receive larger inhibitory currents and display greater decreases in firing rate during SNr axon stimulation, we performed a correlation analysis to evaluate the strength of the relationship among the

synaptic and firing characteristics (**Figure 4L**). Interestingly, there was a weak but significant positive correlation between the PPR and frequency change during stimulation showing that input displaying short-term synaptic depression occurs in neurons with greater decreases in firing frequency (Spearman r=0.486, p=0.030; **Figure 4M**). As expected, SNr-mediated oIPSCs with larger amplitudes are correlated with greater decreases in firing frequency during stimulation (Spearman r=-0.841, p<0.00001; **Figure 4N**). Greater pre-optical stimulation firing frequency is correlated with larger frequency decreases during stimulation (Spearman r=-0.791, p<0.0001; **Figure 4O**). This finding is expected because the fast-firing neurons can be more strongly inhibited in terms of absolute decrease in action potential frequency (i.e. a floor effect). Surprisingly, however, pre-optical stimulation firing frequency is correlated with the first oIPSC amplitude (Spearman r=0.818, p<0.0001; **Figure 4P**), indicating that the SNr is more strongly connected to glutamatergic PPN neurons with faster firing rates. These correlations highlight strong selectivity in SNr projections to PPN glutamatergic neurons. Overall, these findings support that the SNr selectively targets and strongly inhibits fast-firing caudal glutamatergic PPN neurons compared to rostral neurons, and that there is a medial-caudal hotspot where SNr inhibition of PPN glutamatergic neurons is particularly strong.

The SNr most strongly inhibits caudal glutamatergic PPN neurons.

Most of the previous PPN circuit work has been done with rabies tracing. Aside from technical limitations, rabies tracing can only indicate the presence of synaptic connections. Our electrophysiological findings comprehensively characterize the strength and characteristics of the SNr input to each of the PPN cell types in both the rostral and caudal regions. Using this comprehensive dataset, we compared SNr input across the different PPN cell types in each region under the same electrophysiological conditions. We found that the median amplitude of the first SNr-mediated oIPSC was the same among rostral PPN neurons irrespective of cell type [median (IQR); first oIPSC n=15 ChAT+: 74.7 pA (44.5 to 136.5 pA), n=9 Vgat+: 76.5 pA (27.0 to 209.9 pA), n=13 Vglut2+: 61.6 pA (19.2 to 113.9 pA); Kruskal-Wallis, p=0.7046; **Figure 5A**]. The impact of these inhibitory inputs on neuronal firing did not differ with cell type as shown by the absolute change in frequency during SNr stimulation [median (IQR); ΔFrq During Opto n=14 ChAT+: -2.47 Hz (-3.37 to -1.44 Hz), n=7 Vgat+: -5.03 Hz (-5.54 to -1.34 Hz), n=13 Vglut2+: -3.21 Hz (-12.21 to -1.95 Hz); Kruskal-Wallis, p=0.3028; **Figure 5B]**.

We found that the SNr-mediated oIPSCs in caudal glutamatergic neurons were significantly larger than in cholinergic and GABAergic caudal PPN neurons [median (IQR); first oIPSC n=20 ChAT+: 109.3 pA (58.5 to 168.6 pA), n=12 Vgat+: 59.7 pA (37.7 to 269.7 pA), n=13 Vglut2+: 313.5 pA (143.8 to 729.1 pA); Kruskal-Wallis, p=0.0128; Dunn's test, ChAT+ vs Vgat+ p=0.6409, ChAT+ vs Vglut2+ p=0.0042, Vgat+ vs Vglut2+ p=0.0295; **Figure 5C**]. Likewise, the impact of SNr inhibition on neuron firing rate was strongest in caudal glutamatergic neurons. The absolute frequency decrease during stimulation in caudal glutamatergic neurons was larger than both cholinergic and GABAergic neurons [median (IQR); ΔFrq During Opto n=23 ChAT+: -2.10 Hz (-3.11 to -0.84 Hz), n=19 Vgat+: -4.29 Hz (-11.02 to -2.94 Hz), n=17 Vglut2+: -14.08 Hz (-20.04 to -6.07 Hz); Kruskal-Wallis, p<0.0001; Dunn's test, ChAT+ vs Vgat+ p=0.0049, ChAT+ vs Vglut2+ p<0.0001, Vgat+ vs Vglut2+ p=0.0332; **Figure 5D**].

We found no significant difference between SNr-mediated oIPSCs recorded GABAergic and cholinergic neurons in both the rostral and caudal PPN (**Figure 5A&C**). In the caudal PPN, however, the GABAergic neuron firing frequency was more strongly inhibited than cholinergic (**Figure 5D**). The greater reduction in firing frequency may be driven by the caudal GABAergic subgroup receiving particularly large oIPSCs (**Figure 3D**) and could be explained if GABAergic PPN neurons have higher input resistance than cholinergic neurons, as has been previously suggested[57]. Altogether, our findings show that the SNr most strongly inhibits the glutamatergic neurons followed by GABAergic neurons in the caudal PPN and more weakly inhibits rostral PPN neurons without any cell type bias (**Figure 5E**).

The GPe preferentially, but weakly, inhibits a subset of caudal GABAergic and glutamatergic PPN neurons.

GPe projections to the cholinergic and glutamatergic PPN neurons have been shown in previous rabies tracing studies[14–17], but projections to the GABAergic MLR neurons was not detected[14]. To evaluate the synaptic strength of these connections and determine regional connectivity, we repeated the previous whole-cell patch clamp experiments paired with optogenetics, but this time injecting ChR2 into the GPe of ChAT-Cre/Ai9-tdTomato, Vgat-Cre/Ai9-tdTomato, and Vglut2-Cre/tdTomato mice (**Figure 6A**). If oIPSCs were observed in response to optical stimulation, the neuron was identified as connected. In a subset of neurons, a GABA-a receptor blocker, GABAzine, was applied to confirm the oIPSCs were GABA-mediated (See *Methods* for details; **Figure 6B**). We recorded GPe-mediated oIPSCs in all three cell types of the PPN. As predicted by the low density of GPe axons present in the rostral PPN (**Figure 1D**), very few rostral PPN neurons received synaptic input from the GPe. This was true within each molecularly-defined PPN cell type [caudal vs rostral % connected; ChAT+: 30% vs 0% (n=9/30 vs 0/7), Vgat+: 68% vs 38% (n=21/31 vs 6/16), Vglut2+: 69% vs 26% (n=24/35 vs 5/19); **Figure 6Ci-iii**]. These findings suggest that the GPe preferentially targets caudal PPN neurons compared to rostral neurons.

We then tested if the percentage of connected caudal neurons was greater than the percentage of connected rostral neurons. While the caudal connectivity was significantly greater than rostral connectivity in GABAergic and glutamatergic neurons (one-sided Fisher's exact test; Vgat: OR=0.2857, CI=0.09190 to 0.9391, p=0.047; Vglut2: OR=0.1637, CI=0.05069 to 0.5767, p=0.0033; **Figure 6Cii&iii**), we found no statistical difference between the rostral and caudal connectivity in cholinergic neurons (OR=0, CI=0 to 1.301, p=0.1150; **Figure 6Ci**). Because the number of connected caudal cholinergic neurons was not significantly greater than its 0% rostral connectivity (**Figure 6Ci**), GPe inhibition of PPN cholinergic neurons is likely weak to non-existent. Since so few rostral PPN neurons received GPe inhibition, we focused our characterization of GPe inhibition to the caudal PPN.

We then evaluated the strength and impact of GPe inhibition of the few connected caudal cholinergic PPN neurons. First, we measured the amplitude of each oIPSC in the 20 Hz train over 2 seconds. We found that the average oIPSC amplitude across the train was small (approximately 20 pA, **Figure 6D**). Similarly, the first oIPSC measured in the connected cholinergic neurons was also quite small [median (IQR); first oIPSC n=6 ChAT+: 22.6 pA (9.75 to 50.20 pA); **Figure 6E**]. Among recorded caudal cholinergic

PPN neurons, both connected and non-connected, these small inhibitory currents displayed negligible effects on the neuronal firing frequency of the cholinergic PPN population in both the percent of pre-optical stimulation frequency and absolute frequency change [median (IQR); n=29 ChAT+: %Frequency During Stimulation 96.67 % (85.1 to 100.7 %); ΔFrq During Opto -0.16 Hz (-0.90 to 0.03 Hz); **Figure 6H&I**]. These findings indicate that the GPe has essentially no direct effect on the cholinergic PPN neural population as a whole. For this reason, we exclude GPe inhibition of cholinergic PPN neurons in the synaptic characterizations shown in Figures 6F&H. Together, we show that the GPe preferentially inhibits caudal GABAergic and glutamatergic neurons while largely avoiding rostral PPN neurons.

To determine whether the synaptic strength and characteristics from the GPe to the PPN differed between GABAergic and glutamatergic PPN subtypes, we evaluated the amplitude of the GPe-mediated oIPSCs during the 2-second 20 Hz optical stimulation. Because there were few GPe-connected neurons in the rostral PPN, all recorded neurons in these datasets were restricted to the caudal PPN for the analyses in the following paragraphs. Both GABAergic and glutamatergic neurons responded to GPe stimulation with oIPSCs ranging from ones to hundreds of picoamperes (**Figure 6D**). While there was no significant difference in the first oIPSC measured in GABAergic and glutamatergic neurons [median (IQR); first oIPSC n=19 Vgat+: 24.77 pA (6.72 to 54.17 pA), n=15 Vglut2+: 65.71 pA (14.50 to 133.4 pA); Kruskal-Wallis, p=0.2176; **Figure 6E**], the normalized amplitudes show that GPe input to GABAergic neurons facilitates with subsequent stimulations, while the input to glutamatergic neurons depresses (**Figure 6F**). The GPe-mediated inhibitory input to glutamatergic neurons displayed a significantly lower PPR than to GABAergic neurons [median (IQR); PPR n=19 Vgat+: 0.97 (0.76 to 1.2), n=15 Vglut2: 0.81 (0.55 to 0.93); Mann-Whitney, U=76, p=0.0206; **Figure 6G**]. While short-term synaptic plasticity patterns were variable among GABAergic neurons with some depressing and others facilitating, GPe input to glutamatergic neurons generally depresses.

While there was no difference in oIPSC amplitudes, short-term synaptic depression can dampen the impact that repeated IPSCs have on action potential output. Therefore, we compared the firing frequency change in each cell type during optogenetic stimulation of GPe axons. As expected, the inhibition of action potential firing in both GABAergic and glutamatergic neurons was significantly greater than the overall GPe inhibition of cholinergic neurons (mean ± SEM; %Frequency During Stimulation n=25 ChAT+: 92.39 ± 7.59 %, n=18 Vgat+: 57.70 ± 10.11 %, n=29 Vglut2+: 64.15 ± 7.63 %; 2way ANOVA, p=0.0302; Tukey test, During Stimulation ChAT+ vs Vgat+ p=0.0359, ChAT+ vs Vglut2+ p=0.0391, Vgat+ vs Vglut2+ p=0.8669; Pre vs During ChAT+ p=0.5818, Vgat+ p=0.0017, Vglut2+ p=0.0002; median (IQR); ΔFrq During Opto n=25 ChAT+: -0.16 Hz (-0.90 to 0.03 Hz), n=18 Vgat+: -1.92 Hz (-3.85 to -0.60 Hz), n=29 Vglut2+: -0.89 Hz (-3.28 to -0.43 Hz); Kruskall-Wallis, p=0.0002; Dunn's test, ChAT+ vs Vgat+ p=0.0002, ChAT+ vs Vglut2+ p=0.0009, Vgat vs Vglut2+ p=0.4020; **Figure 6H&I**). The PPN GABAergic neuron population firing rate was decreased to about 58% of their pre-stimulation firing with a median frequency decrease of 1.92 Hz during stimulation (**Figure 6H&I**). Similarly, the glutamatergic neuron population firing rate was decreased to about 64% of their pre-stimulation firing with a median frequency decrease of 0.89 Hz during stimulation (**Figure 6H&I**). We found no statistical difference between

GPe inhibition of firing frequency in caudal GABAergic and glutamatergic PPN neurons. These findings show that the GPe inhibits GABAergic and glutamatergic neural populations to a similar extent.

To determine if there are significant relationships among the synaptic and firing characteristics, we performed a correlation analysis. Among GABAergic neurons receiving GPe inhibition, we found that the amplitude of the first oIPSC is significantly correlated with the absolute change in frequency during stimulation (Spearman r=-0.627, p=0.044, **Figure 6K**). Although GPe input to GABAergic neurons exhibited various PPRs, the correlation analyses revealed no significant relationship between PPR and absolute change in frequency during stimulation (**Figure 6J**). These findings suggest that the initial oIPSC amplitude of GPe input to GABAergic PPN neurons has a stronger relationship with firing rate than short-term synaptic plasticity does.

As nearly all GPe inputs to glutamatergic neurons exhibited short-term synaptic depression, we expected the correlation analysis to reveal a significant relationship between PPR and the change in firing frequency. However, similar to the GPe input to GABAergic neurons, PPR was not predictive of impact on neuronal activity (**Figure 6L**). GPe inhibition of the glutamatergic neurons showed a significant correlation between the absolute change in frequency during stimulation and pre-stimulation firing frequency (Spearman r=-0.648, p=0.014, **Figure 6M**). However, because the inhibitory synaptic current amplitude did not correlate with firing frequency, this correlation is likely due to a floor effect in which faster firing neurons have a greater capacity for reductions in firing frequency. Together, these findings suggest that the GPe preferentially inhibits caudal GABAergic and glutamatergic PPN neurons.

In vivo activation of GPe and SNr axons in the PPN show opposite effects on locomotion and valence.

Once we established that the SNr and GPe inhibit different profiles of regionally- and molecularly-defined subpopulations of the PPN using *ex vivo* optogenetic electrophysiology, we wanted to evaluate the behavioral consequences of selectively stimulating these inputs *in vivo*. Direct optogenetic activation of PPN subpopulations have been previously shown to either promote or inhibit motion, sometimes with contradictory results[14,16,17,22–27]. To determine whether differential inhibitory inputs onto the PPN influenced locomotor activity, we bilaterally injected wild-type mice with ChR2 in either the SNr or GPe and implanted an optical fiber over the PPN (**Figure 7A&B**). Control mice were injected with an EGFP virus and implanted. After three weeks, we placed each mouse in the open field to measure gross locomotor behavior with and without optical stimulation of the SNr or GPe axons. We tracked the distance traveled for each mouse at baseline and during bilateral stimulation of either the SNr or GPe by applying blue light (473 nm, 4-4.5 mW) at 20 Hz with 2 ms pulses (4% duty cycle), for 1 minute at a time (**Figure 7C**). We found that stimulation of these two inhibitory basal ganglia inputs to the PPN resulted in completely opposite motor behaviors. Specifically, stimulation of SNr axons in the PPN increased distance traveled, while stimulation of GPe axons in the PPN decreased distance traveled [mean ± SEM; N=9 (3M, 6F) Control (Ctrl): 2.22 ± 0.24 m, N=8 (5M, 3F) SNr: 4.11 ± 0.51 m, N=9 (4M, 5F) GPe: 0.57 ± 0.18 m; Welch ANOVA, Dunnett's test, p<0.0001; Ctrl vs SNr p=0.0138, Ctrl vs GPe p=0.0001; **Figure 7D**, see Video S1&2].

The PPN has been implicated in reward processing and stimulation of the PPN can be reinforcing[7,27,28,30,34,58]. Therefore, we evaluated the effect of GPe or SNr axon stimulation in the PPN on valence in the real-time place preference (RTPP) task. In a three-chamber apparatus, the mouse could freely move between chambers for ten minutes. Optical stimulation of the SNr or GPe axons in the PPN was applied when the mouse entered the stimulated chamber and remained on at 20 Hz (4% duty cycle) until the mouse exited that chamber (**Figure 7E**). To reduce the effects of optical stimulation on locomotion, this experiment was conducted with unilateral stimulation only. Interestingly, we again found opposite effects when stimulating the two inhibitory basal ganglia inputs to the PPN. Mice avoided the stimulated chamber when the SNr axons were stimulated, but preferred the stimulated chamber when the GPe axons were stimulated (mean ± SEM; N=16 (6M, 10F) Ctrl: 40.76 ± 2.0 %, N=9 (5M, 4F) SNr: 23.99 ± 5.2 %, N=10 (5M, 5F) GPe: 76.11 ± 3.7 %; One-way ANOVA, $p<0.0001$; Dunnett's test, Ctrl vs SNr $p=0.0025$, Ctrl vs GPe $p<0.0001$; **Figure 7F**, see Video S3&4).

In addition to sending inhibitory inputs to the PPN, the GPe and SNr send axon collaterals to multiple other brain areas[12,36,59,60]. Therefore, it is possible that stimulating these axons in the PPN could cause antidromic stimulation of the GPe and SNr cell bodies, resulting in the inhibition of non-PPN brain regions. However, it has recently been shown that 0.25 mW laser power stimulation of axons can prevent antidromic activation of cell bodies[41]. Therefore, we repeated these optogenetic behavioral experiments using 0.25 mW laser power. We found that the locomotion effect of SNr stimulation over the PPN was no longer present during low power stimulation, but GPe stimulation still significantly decreased locomotion (mean ± SEM; distance traveled N=9 (3M, 6F) Ctrl: 2.22 ± 0.24 m, N=6 (3M, 3F) SNr: 2.24 ± 0.50 m, N=8 (4M, 4F) GPe: 1.09 ± 0.22 m; One-way ANOVA, $p=0.0211$; Dunnett's test, Ctrl vs SNr $p=0.9993$, Ctrl vs GPe $p=0.0232$; **Figure 7H**). In the RTPP task, SNr axon stimulation continued to evoke place aversion and GPe axon stimulation continued to evoke place preference (mean ± SEM; % time in stimulation zone N=16 (6M, 10F) Ctrl: 40.76 ± 2.1 %, N=6 (3M, 3F) SNr: 27.72 ± 4.0 %, N=8 (4M, 4F) GPe: 68.41 ± 8.5 %; Welch's ANOVA, $p=0.0044$; Dunnett's test, Ctrl vs SNr $p=0.0378$, Ctrl vs GPe $p=0.0252$; **Figure 7G**). These findings show that decreased locomotion and place preference are mediated by GPe inhibition of the PPN. Interestingly, we find that aversion is mediated by SNr inhibition of the PPN, but the enhancement of locomotion is likely due to PPN-projecting SNr neurons inhibiting a separate brain structure.

Discussion:

In this study, we comprehensively characterize the synaptic strength and impact on neuron action potential firing in molecularly- and regionally-defined PPN subpopulations while stimulating the SNr or GPe using *ex vivo* electrophysiology and optogenetics. We also stimulated the SNr or GPe axons in the PPN *in vivo* which revealed SNr and GPe populations, defined by their projections to the PPN, involved in non-canonical basal ganglia circuits to evoke opposing locomotion and valence processing behaviors. Together, these findings show that distinct and selective inhibition of PPN subpopulations by the SNr and GPe can alter behavioral output.

Region- and cell type-specific inputs to the PPN

The SNr and GPe have been previously shown to form monosynaptic synapses with PPN neurons using rabies viral tracing[12–17]. While SNr input to cholinergic and glutamatergic PPN neurons has been reproduced across different studies[13–17], SNr inputs to GABAergic PPN neurons has only been inferred from studies of the entire mesencephalic locomotor region (MLR), consisting of both the PPN and cuneiform nucleus[14]. Several studies have used slice electrophysiology to show that the SNr inhibits PPN neurons generally[31] or to compare SNr input to cholinergic and non-cholinergic PPN neurons[47,50,51]. However, a full characterization of the SNr input to regionally- and molecularly-defined PPN neurons in adult animals has been lacking. Using *ex vivo* whole-cell patch recordings, we were able to measure inhibitory currents in each of the PPN cell types during SNr stimulation showing that the SNr functionally inhibits each cell type within the rostral PPN to a similar extent while most strongly inhibiting a medial-caudal 'hotspot' of glutamatergic neurons.

While the GPe has been shown to project to the cholinergic and glutamatergic PPN neurons[15–17], our electrophysiological results show that GPe inhibition of the cholinergic neurons is weak to non-existent and its inhibition of the glutamatergic PPN neurons is caudally biased. In contrast to a previous study showing that the GPe does not project to GABAergic MLR neurons[14], we find that the GPe also preferentially inhibits a caudal subgroup of GABAergic PPN neurons. While the GPe selectively inhibits a caudal subpopulation of GABAergic and glutamatergic PPN neurons, its inhibition is much weaker than SNr inhibition of the PPN in terms of the proportion of connected PPN neurons, the inhibitory current amplitudes, and the inhibition of neuronal firing. Overall, our findings utilize a systematic approach to characterize the synaptic strength between these inhibitory basal ganglia nuclei and the PPN across its rostrocaudal axis for each cell type allowing us to compare SNr and GPe to PPN circuitry with regional-level granularity. These results also encourage future work involving the PPN to consider the individual influence of its rostral and caudal regions.

Noncanonical basal ganglia motor circuits

We found that stimulation of GPe axons over the PPN decreased locomotion in both low (local) and high (putatively generating antidromic activity) laser power stimulations, while only high power SNr axon stimulation increased locomotion. This suggests that antidromically activating the subpopulation of SNr neurons that project to the PPN is required to generate the non-canonical increase in locomotion, but that this locomotion increase is not due to the SNr inhibition of the PPN. These behavioral outcomes appear counter to the canonical model of basal ganglia movement pathways, in which SNr activation decreases and GPe activation increases movement. Although there is strong support for this canonical model, recent *in vivo* recordings have found subpopulations of SNr and GPe neurons that show activity patterns counter to this model (i.e., SNr neurons that increase activity during movement and GPe neurons that increase activity during immobility)[61–67]. Similarly, a subset of SNr and GPe neurons paradoxically increase activity upon direct and indirect pathway striatal projection neuron stimulation, respectively[40,68]. While one explanation for these heterogeneous responses could be local inhibition within each structure[39,40,69–73], another possibility is that distinct subpopulations within the SNr and GPe differentially modulate locomotor

behavior[12,33,38–40,59,63,71]. Our findings support non-canonical basal ganglia motor pathways involving SNr and GPe neurons that project to the PPN.

Our characterization of region-specific inhibitory inputs to the PPN helps us understand how GPe inhibition of the PPN can mediate decreases in locomotion. Our electrophysiology experiments show that the GPe exerts minimal influence on the rostral PPN neurons which appear to decrease locomotion[22,24] and preferentially inhibits caudal GABAergic and glutamatergic PPN neurons. Because stimulating the caudal GABAergic and glutamatergic PPN neurons increases locomotion[23], GPe selective inhibition of these caudal neurons could explain our behavioral experiments showing that stimulation of GPe axons over the PPN decreases locomotion. Aligned with our findings, selectively stimulating the Npas1+ or FoxP2+ subpopulations in the GPe decreases locomotion[38,40]. Some groups have found that direct stimulation of the PV+ GPe neurons increases locomotion[38,60]; however, one study shows that inhibition of PV+ GPe neurons can increase locomotion[41]. While we show that GPe projections to the PPN decrease locomotion, future studies are needed to determine which GPe subpopulations project to the PPN to modulate locomotion.

While we found that stimulating SNr axons in the PPN with high laser power increased locomotion, we observed no locomotor effect when using low laser power stimulation. Therefore, our findings suggest that antidromic activation of the PPN-projecting SNr neuron subpopulation during high laser power stimulation promotes locomotion, but not through direct actions at the PPN. Previous studies have identified distinct functional roles for molecularly-defined subpopulations within the SNr. Although direct stimulation of PV+ and GAD2+ SNr neurons decreases gross locomotor movement[33,63], PV+ SNr neurons have been shown to increase their activity during transitions from quiet wakefulness to non-locomotor movement[63]. The subset of PV+ and GAD2+ SNr neurons which project to the PPN also broadly project to other SNr output targets[12,63] whose inhibition may mediate increases in locomotion. However, stimulation of SNr neurons has not previously been shown to increase locomotion. One possibility is that the adjacent dopaminergic neurons of the substantia nigra *pars compacta* (SNc) are infected with ChR2 in our experiments. Some SNc dopaminergic neurons send axons to both the PPN and striatum[74]. Because direct stimulation of nigrostriatal neurons increases locomotion[75], antidromic stimulation of the SNc can evoke dopamine release into the striatum to increase movement in our high laser power experiments. However, we also find that this high-power SNr axon stimulation is highly aversive (Figure 7F). Because dopaminergic neuron activation is usually rewarding, our aversive effect does not support antidromic activation of these dopaminergic neurons. Our findings suggest the existence of a SNr subpopulation, defined by their projections to the PPN, that can positively modulate movement. However, future work is needed to test the locomotor effects of direct stimulation of PPN-projecting SNr neurons.

Differential inhibition of PPN subpopulations by the SNr and GPe mediate opposing valence processing outcomes

We found that stimulation of SNr axons over the PPN was aversive in real time place preference (RTPP), while stimulation of GPe axons over the PPN led to increased preference for the stimulated chamber. Previous studies directly stimulating SNr and GPe subpopulations have implicated these structures in reward and aversion

processing. Inhibition of Vgat+ SNr neurons has been shown to increase place preference[35] while its direct stimulation has no effect[33,35]. However, selective stimulation of the PV+ SNr neurons induces aversion in RTPP[33]. Although the GPe has been predominantly studied in the context of movement, recent work has begun to reveal a role for the GPe in valence processing[41,76–78]. One recent study shows that inhibition of PV+ GPe neurons induced aversion while inhibition of Npas1+ GPe neurons induced placed preference in RTPP[41]. Because activation of PV+ SNr neurons is aversive[33] and inhibition of PV+ GPe neurons is aversive[41], it is likely that our results are due to activation of the PV+ SNr and GPe axons in the PPN. While we show that activation of the PPN-projecting SNr and GPe subpopulations strongly affect valence processing, future studies are needed to determine whether these effects are specifically mediated by PV+ SNr and GPe projections to the PPN.

Neurons in the PPN have been implicated in reward and aversive-related behaviors[7,27,28,30–32,34,58]. The cholinergic PPN neurons are implicated in positive valence with place preference and increased lever pressing through their projections to the ventral tegmental area (VTA)[27,28]. Aligned with our findings, direct inhibition of the cholinergic PPN neurons evokes place aversion[27]. Of particular significance, we show that the SNr inhibits the cholinergic PPN neurons while the GPe axons avoid cholinergic PPN neurons. Therefore, it is possible that the difference between the SNr and GPe effects on valence is due to their differential inhibition of the cholinergic PPN neurons.

Direct stimulation of the glutamatergic PPN neurons has also been implicated in positive valence with increased reinforcement behavior[7]. Both the cholinergic and glutamatergic PPN neurons directly influence dopamine release in the striatum and dopaminergic neuron activity in the SNc and VTA[7,27,28,79–83]. Specifically, the caudal PPN neurons are thought to innervate the medial part of the SNc and the VTA[9,83], two major reward pathway hubs. Our data show that the SNr most strongly inhibits the caudal glutamatergic PPN neurons. Therefore, strong SNr inhibition of these neurons would remove excitatory drive from the reward-related dopaminergic neurons. This pathway could also contribute to the aversive effect of SNr axon stimulation in the PPN.

The pathways underlying the GPe-mediated rewarding effect are less clear and may indicate functional heterogeneity among caudal PPN neurons. We find that the GPe only inhibits a subset of caudal GABAergic and glutamatergic PPN neurons. It is possible that the subset of GABAergic PPN neurons targeted by the GPe disinhibits local cholinergic and glutamatergic neurons to increase excitation of the rewarding dopaminergic neuron pathways. Another possibility is that the specific GPe-inhibited PPN population may have particularly aversive-properties. For example, PPN neurons that excite amygdala nuclei evoke place avoidance[34,58]. In this case, GPe inhibition of these neurons could be rewarding by removing excitation of amygdala nuclei involved in negative valence processing. Future experimental work is needed to determine the extent of local inhibition among PPN neurons and define the characteristics of the PPN neurons selectively targeted by the GPe.

Conclusions

We have systematically characterized SNr and GPe inputs across the rostrocaudal axis of the PPN for each cell type – cholinergic, GABAergic, and glutamatergic. We show that the SNr inhibits nearly every PPN cell recorded with differential strength

720 determined by cell type and anatomical biases while identifying a medial-caudal
721 'hotspot' of glutamatergic neurons most strongly inhibited by the SNr. In contrast, the
722 GPe strikingly avoids the cholinergic PPN neurons and more weakly, but selectively,
723 inhibits a subpopulation of caudal GABAergic and glutamatergic neurons. We proposed
724 that the differential inhibition of regionally-biased, mixed-cell type PPN subpopulations
725 can alter behavioral outputs. By stimulating these inhibitory basal ganglia axons over
726 the PPN, we show that the SNr evokes place aversion while the GPe evokes place
727 preference and decreases locomotion. Surprisingly, we find that high laser power
728 stimulation (likely to evoke antidromic activation) of PPN-projecting SNr neurons
729 increases locomotion. Together, our findings show that the SNr and GPe mediate
730 opposing valence processing outcomes through the PPN and support non-canonical
731 basal ganglia motor pathways in which the PPN-projecting SNr subpopulation increases
732 locomotion and the GPe decreases locomotion through its projections to the PPN.
733
734 **Acknowledgements:**
735 Funding for this research was provided by an NIH BRAIN Initiative grant R00NS112417
736 (to RCE), NIH NINDS grant F30NS132399 (to MF), Michael J Fox Foundation Research
737 Grant MJFF-022863 (to RCE), and Parkinson's Foundation Summer Student Fellowship
738 PF-SSF-941810 (to AES). This research was supported by the Microscopy and Imaging
739 Shared Resource (MISR, S10RR025661) and the Lombardi Comprehensive Cancer
740 Center grant (P30-CA051008). We would like to thank the Division of Comparative
741 Medicine for their animal care and management and Dr. Stefano Vicini, Dr. Aryn Gittis,
742 and members of the Evans lab for their feedback on earlier versions of this manuscript.
743
744 **Author Contributions:**
745 M.F. and R.C.E. conceptualized the experiments; M.F. performed stereotaxic injections,
746 conducted the electrophysiological experiments, and analyzed the data; A.E.S. and
747 K.C.U. performed stereotaxic injections, conducted the behavioral experiments, and
748 analyzed the data; C.B.S. performed stereotaxic injections for pilot experiments; M.F.
749 wrote the initial draft of the manuscript; M.F. and R.C.E. edited and revised the
750 manuscript.
751
752 **Declaration of Interests**
753 The authors declare no competing interests.
754
755
756 **Star Methods text**
757 **KEY RESOURCES TABLE**

REAGENT or RESOURCE	SOURCE	IDENTIFIER
Antibodies		
goat anti-choline acetyltransferase (ChAT)	Millipore	Cat#: AB144P, RRID: AB_2079751
Streptavidin, Cy5	Invitrogen	Cat#: SA1011
Streptavidin, DyLight™ 405	Invitrogen	Cat#: 21831
Donkey anti-goat IgG (H+L) Cross-Adsorbed Secondary Antibody, Alexa Fluor™ 647	Invitrogen	Cat#: A-21447, RRID: AB_2535864

Sheep anti-tyrosine hydroxylase (TH)	Novus Biologicals	Cat# NB300-110, RRID: AB_10002491
DyLight™ 405 AffiniPure™ Donkey Anti-Sheep IgG (H+L)	Jackson ImmunoResearch Laboratories	Cat# 713-475-147, RRID: AB_2340740
Bacterial and virus strains		
AAV1-hSyn-hChR2(H134R)-EYFP	Addgene (Deisseroth Lab)	Cat#: 26973
AAV1-hSyn-EGFP	Addgene (Roth Lab)	Cat#: 50465
Chemicals, peptides, and recombinant proteins		
D-AP5	Tocris and HelloBio	Cat#: 0106 and HB0225
NBQX	Tocris and HelloBio	Cat#: 1044 and HB0443
CNQX disodium salt	HelloBio	Cat#: HB0205
SR 95531 hydrobromide (GABAzine)	Tocris and HelloBio	Cat#: 1262 and HB0901
Experimental models: Organisms/strains		
ChAT-cre mice: B6.129S-Chat$^{tm1(cre)Lowl}$/MwarJ	Jackson	RRID: IMSR_JAX:031661
Vgat-cre mice: B6J.129S6(FVB)-*Slc32a1*$^{tm2(cre)Lowl}$/MwarJ	Jackson	RRID: IMSR_JAX:028862
Vglut2-cre mice: B6J.129S6(FVB)-Slc17a6$^{tm2(cre)Lowl}$/MwarJ	Jackson	RRID: IMSR_JAX:028863
Ai9-tdTomato mice: B6.Cg-Gt(ROSA)26Sor$^{tm9(CAG-tdTomato)Hze}$/J	Jackson	RRID: IMSR_JAX:007909
C57BL/6J	Jackson	RRID: IMSR_JAX:000664
Software and algorithms		
Igor Pro	WaveMetrics	Version 9.00
GraphPad Prism	Dotmatics	Version 9.5.0
Fiji software	Open source on GitHub	Version 1.51n
ANY-maze® software	Stoelting Company, Wood Dale, IL.	Version 7.36
Clampex software	Molecular Devices	Version 11.2
Other		
Multiclamp™ 700B amplifier		
Axon™ Digidata® 1550B		
Leica SP8AOBS++		
Zeiss Axio Imager Z2		
Sutter Instrument Model P-97		

RESOURCE AVAILABILITY

Lead contact

Further information and requests for resources and reagents should be directed to and will be fulfilled by the lead contact, Dr. Rebekah C. Evans (re285@georgetown.edu).

Materials availability

This study did not generate new unique reagents.

Data and code availability

- All data and code supporting the current study will be shared by the lead contact upon request.
- No original code was generated in this paper.
- Any additional information required to reanalyze the data reported in this paper is available from the lead contact upon request.

EXPERIMENTAL MODEL AND STUDY PARTICIPANT DETAILS

Animal Welfare

All animal procedures were approved by the Georgetown University Medical Center Institutional Animal Care and Use Committee (IACUC). Measures were taken to ensure minimal animal suffering and discomfort, and protocols were designed to minimize the number of animals used.

Animal Subjects

Homozygous Ai9-TdTomato mice [B6.Cg-Gt(ROSA)26Sor$^{tm9(CAG-tdTomato)Hze}$/J; JAX# 007909] were bred with homozygous ChAT-Cre mice [B6.129S-Chat$^{tm1(cre)Lowl}$/MwarJ; JAX# 031661], homozygous Vgat-Cre mice [B6J.129S6(FVB)-*Slc32a1*$^{tm2(cre)Lowl}$/MwarJ; JAX# 028862], and Vglut2-Cre mice [B6J.129S6(FVB)-Slc17a6$^{tm2(cre)Lowl}$/MwarJ; JAX# 028863] to obtain ChAT-Cre/Ai9-tdTomato, Vgat-Cre/Ai9-tdTomato, and Vglut2-Cre/Ai9-tdTomato in-house, respectively. C57BL/6J wildtype mice (Jax# 000664) were obtained from Jackson for behavioral experiments. Animals were housed under a 12:12 light-dark cycle (lights on at 06:00 AM) with food and water *ad libitum*.

Experimental Groups

For electrophysiological studies, ChAT-Cre/Ai9-tdTomato, Vgat-Cre/Ai9-tdTomato, and Vglut2-Cre/Ai9-tdTomato mice of both sexes (3 males and 3 females in each group) aged 2-5 months were used. For behavioral studies, C57BL/6J wildtype mice of both sexes, with age-matched littermates randomly assigned to control or experimental groups. Behavioral assessments were exclusively conducted during the light phase, and all testing chambers were cleaned with 70% ethanol between mice to mitigate potential olfactory influences.

METHOD DETAILS

Viral injections and optical fiber implantation surgeries

Mice at least 7 weeks old were briefly anesthetized with inhaled 5% isoflurane using an anesthetic chamber and placed onto a heated pad within the stereotaxic frame (Stoelting 51730UD). The skull was stabilized with evenly positioned ear bars and nose cone properly positioned to deliver continuous 1-3% isoflurane and oxygen at a steady flow of 1L/min throughout the surgery duration. Bupivacaine (5 mg/kg) and carprofen (5mg/kg) were administered as local anesthetic and analgesic, respectively. A small incision was made on the scalp to visualize bregma and lambda, which were used as references to level the skull. Bilateral holes were drilled at either the coordinates of the SNr (AP -3.1 mm, ML ± 1.4 mm, DV -4.7 mm relative to bregma) or GPe (AP -0.3 mm, ML ± 1.9mm, DV -3.9 mm relative to bregma). The 5µL Hamilton microsyringe was positioned and 250 nL virus was injected at a rate of 0.2 µL/min. The syringe was raised and rested 0.5 mm above the injection site for 10 minutes. For *ex vivo* optogenetic experiments, AAV1-hSyn-hChR2(H134R)-EYFP (2.3 x 10^13 particles per milliliter, Addgene, Cat# 26973) was injected into either the SNr or GPe. For *in vivo* optogenetic experiments, AAV1-hSyn-hChR2(H134R)-EYFP 2.0 x 10^13 particles per milliliter, Addgene, Cat #26973) or AAV1-hSyn-EGFP (1.1 x 10^13 particles per milliliter, Addgene, Cat# 50465) was injected into either the SNr or GPe for experimental and control mice, respectively. For mice used in the *in vivo* optogenetic experiments, an optical fiber (200 µm core, 0.22 NA, 3.7 mm length) was implanted over the PPN (AP -4.5, ML ± 1.1 mm, DV -3.5 relative to bregma). The skin on either side of the incision site was joined, glued together using VetBond tissue adhesive, and fastened with two wound clips or the optical fiber was fixed in position with dental cement. (C&B-Metabond Quick! Adhesive Luting Cement by Parkell Products Inc, Patterson# 553-3484/CAT# S380; Jet Denture Repair Package by LANG, CAT# 1223F2). Post-surgery, buprenorphine SR (1.5 mg/kg) was administered for long-acting analgesia. Mice were allowed to recover on a heating pad until fully awake and were monitored daily for signs of distress or infection.

Electrophysiological solutions

Acute brain slices were prepared in modified artificial cerebrospinal fluid (aCSF) solutions with final osmolarities ~300-310 mOsm and ~7.4 pH. The slicing solution contained (in mM) 198 glycerol, 2.5 KCl, 1.2 NaH_2PO_4, 20 HEPES, 25 $NaHCO_3$, 10 glucose, 10 $MgCl_2$, and 0.5 $CaCl_2$. The holding solution contained (in mM) 92 NaCl, 2.5 KCl, 1.2 NaH_2PO_4, 30 $NaHCO_3$, 20 HEPES, 2 $MgCl_2$, 2 $CaCl_2$, 35 glucose, 5 sodium ascorbate, 3 sodium pyruvate, and 2 thiourea. Recording aCSF was made up of (in mM): 125 NaCl, 25 $NaHCO_3$, 3.5 KCl, 1.25 NaH_2PO_4, 10 glucose, 1 $MgCl_2$, 2 $CaCl_2$. Whole-cell patch clamp recordings used a potassium methane sulfonate ($KMeSO_3$)-based internal solution containing (in mM) 122 methanesulfonic acid, 9 NaCl, 9 HEPES, 1.8 $MgCl_2$, 4 Mg-ATP, 0.3 Tris-GTP, and 14 phosphocreatine for a final osmolarity between 290 and 305 mOsm. The internal solution contained neurobiotin (0.1-0.3%) for post-hoc staining. These reagents enable reliable electrophysiology recordings in adult brainstem neurons[45,84].

Slicing and Electrophysiology

Animals were anesthetized with inhaled isoflurane and transcardially perfused with ice-cold slicing solution that had been bubbled with 95% O_2 and 5% CO_2. Mice were decapitated and brains were quickly extracted from the skull, keeping the cerebellum intact. For sagittal slices, the brain hemispheres were separated and the medial side was glued onto a 3% agar block fixed to the stage of a semi-automatic Leica VT1200 microtome. 200 µm-thick slices were obtained and incubated at 34°C in holding solution for 30 minutes then kept at room temperature. In all steps, the modified aCSF solutions are bubbled with 95% O_2 and 5% CO_2. Slices in recording chamber during whole-cell patch clamp experiments were continuously perfused with oxygenated recording aCSF kept at 28-34°C using a water bath and in-line Warner heater. Cells were visualized using an Olympus OpenStand upright microscope and 565nm ThorLabs LED light. Recording pipettes with resistance between 1.5-4 MΩ were prepared using borosilicate glass capillaries (World Precision Instruments, Inc. 1B150F-4, 4-inch length, 1.5 mm OD, 0.84 mm ID) with a micropipette puller (Sutter Instrument Model P-97). Recordings were obtained using a Multiclamp™ 700B amplifier and Axon™ Digidata® 1550B controlled by Clampex 11.2. Voltage-clamp signals were low-pass filtered at 2kHz and sampled at 10 kHz. Current-clamp signals were low-pass filtered at 10kHz and sampled at 10 kHz. At the end of recording, the cell was sealed by moving the recording pipette slightly above the soma and an image was taken of the PPN and pipette tip.

***Ex vivo* optogenetic activation**

Whole-field optogenetic activation of channelrhodopsin-infected axons in brain slice was achieved with a blue (470 nm) ThorLabs LED light sent to the tissue via a silver mirror. Light intensity measured at the objective back aperture was 13 mW. Light activation was applied at 20 Hz with 2 ms pulse intervals for 2 seconds. All recordings were conducted in the presence of glutamatergic receptor blockers – 50µM D-AP5 (Tocris Cat#0106 and HelloBio Cat#H0225), and 5µM NBQX (Tocris Cat#1044 and HelloBio Cat#HB0443) alone or in combination with 20µM CNQX (HelloBio Cat#HB0205).

In voltage-clamp, cells were determined to be connected if observable optically evoked inhibitory post synaptic currents (oIPSCs) were measured while holding the cell at -50 mV. In a subset of neurons, 10µM GABAzine (Tocris Cat#1262 and HelloBio Cat#HB0901) was applied to ensure the oIPSCs were GABA-a receptor mediated. In a few cells (17/54), small inhibitory currents remained with amplitudes averaging about 24% of the first oIPSC measured. Any cells that required greater than 200pA to be held at -50mV or that had access resistance that exceeded 30 MΩ at the start of recording were excluded from oIPSC quantitative analyses as they were likely unhealthy and too leaky; however, the first oIPSC amplitude was used as an approximate measure of input strength in the cell maps (SNr: 21/46; GPe: 11/40). oIPSC amplitudes were measured from the baseline to the peak of each current. The paired pulse ratio (PPR) was calculated from the amplitudes of the first two currents evoked in the 20 Hz train.

For current-clamp recordings, most patched PPN neurons spontaneously fired, but a few required a small amount of hyperpolarizing or depolarizing current to fire [(R)ostral, (C)audal; SNr-PPN_{ChAT} R: 3/14, C: 4/23; SNr-PPN_{Vgat} R: 2/7, C: 9/19; SNr-PPN_{Vglut2} R: 2/13, C: 1/17; GPe-PPN_{ChAT} R: 2/7, C: 9/25; GPe-PPN_{Vgat} R: 2/7, C: 8/18; GPe-PPN_{Vglut2} R: 6/12, C: 7/29 required current). Neurons injected with more than 60 pA were excluded. In this manuscript, we use “pre-stimulation firing frequency” to refer to the time period right before optical stimulation. The pre-stimulation firing frequency was measured using the number of action potentials in the one-second epoch before the start of stimulation. The firing frequency during stimulation was measured using the middle one-second of the 2-second stimulation. The post-

stimulation firing frequency was measured in the one-second epoch immediately following the end of the stimulation. The absolute frequency change is the difference between the pre-simulation and during stimulation frequencies. The rebound frequency change is the difference between the post-stimulation and pre-stimulation frequencies. These values include cells with and without holding current applied. By contrast, the spontaneous firing rate of the cell includes only cells with no holding current applied.

***In vivo* optogenetic activation**

Two behavioral tests the open field (OF) test and real-time place preference (RTPP) were conducted sequentially to assess gross locomotion and place preference. Optical stimulation was achieved by the application of blue light (473 nm) at 20 Hz with 2 ms pulses (4% duty cycle). Behavioral testing was conducted under both high laser power (4.0-4.5 mW) and low laser power (0.2-0.25 mW) conditions. Low power testing was employed to control for potential behavioral effects related to antidromic stimulation. On day 1, mice underwent OF testing and were randomly assigned to high or low power stimulation conditions. On day 2 mice were tested in the open field arena for a second time under opposite power conditions. On day 3 mice were tested in the RTPP arena and were again randomly assigned to high or low power conditions. On day 4, mice were tested in the RTPP arena without any stimulation to assess retention of place memory. Finally, on day 5, mice underwent RTPP under opposite power conditions (low vs high) and opposite chamber as stimulation zone (stripes vs spots) to those on Day 3.

Open Field Test

OF test was conducted in an opaque arena measuring 40.64 x 40.64 x 40.64 cm. Animals were placed in the center of the arena and allowed to explore freely for 10 minutes. This was followed by 5 minutes of discontinuous bilateral photostimulation at either high or low power, 5 minutes of recovery, another 5 minutes of discontinuous photostimulation at 20 Hz (at either high or low power), and a final 5 minutes of recovery. The discontinuous photostimulation consisted of three 1-minute photostimulation periods interspersed with 1-minute intervals of no photostimulation. Movement during the OF test were recorded and analyzed using ANY-maze® software (Stoelting Company, Wood Dale, IL).

Real-Time Place Preference

The real-time place preference (RTPP) apparatus consisted of a rectangular behavioral arena with three chambers, each measuring 24.60 x 27.94 x 27.94 cm, with a non-reflective grey background. The adjacent chambers had distinct visual cues: one chamber featured stripes and the other spots. These striped and spotted zones were randomly assigned as stimulation zones between animals. The center chamber and one of the adjacent chambers served as neutral zones, while the other adjacent chamber served as a stimulation zone. Animals received unilateral optical stimulation when in the assigned stimulation zone. To mitigate locomotor effects with bilateral stimulation, unilateral optical stimulation was used in RTPP. Individual subjects were placed in the RTPP apparatus and allowed 10 minutes to explore both compartments. The time spent in each compartment was recorded in real-time using ANY-maze® software (Stoelting Company, Wood Dale, IL).

Immunohistochemistry and confocal imaging

After electrophysiological experiments, brain slices were fixed overnight in a 4% w/v paraformaldehyde (PFA) solution in phosphate buffer (PB) solution, pH 7.6 at 4^{o}C. The fixed brain slices were then stored in phosphate buffer (PB) solution until immunostaining.

Brain slices were also collected at the conclusion of behavioral experiments. Mice were deeply anesthetized and perfused with phosphate buffer (PB), followed by a fixative solution containing 4% w/v paraformaldehyde (PFA) in PB, pH 7.6, at 4°C. Whole brains were extracted and fixed overnight in the same PFA solution. After fixation, brains were stored in PB solution until further processing. For cubic processing, 200 µm-thick sagittal slices were obtained from post-behavioral whole mouse brains using the PELCO easiSlicer™ Vibratory Tissue Slicer.

A CUBIC tissue clearing protocol [42] was combined with immunofluorescence staining as in[84] for all fixed brain slices from both electrophysiological and behavioral experiments. All steps are performed at room temperature on a shaker. Slices were placed in CUBIC reagent 1 for 1-2 days; then washed in PB 3x for 1 hour each; placed in blocking solution (0.5% fish gelatin in PB) for 3 hours; placed in primary antibodies for 2-3 days; washed in PB 3x for 2 hours each; placed in secondary antibodies for 2-3 days; washed in PB 3x for 2 hours each; and placed in CUBIC reagent 2 for 2 hours before mounting onto

slides (Fisherbrand 12-550-403) in reagent 2 and sealed with frame-seal incubation chambers **(**Thermo Scientific AB-0577) and a coverslip (Corning 2845-18).

Neurobiotin-filled patched neurons were stained with streptavidin antibody (Cy5, Invitrogen Cat#SA1011, 1:1000 or DyLight™ 405, Invitrogen Cat#21831, 1:1000). Goat anti-ChAT primary antibody (Sigma Cat#AB144P, 1:200) and donkey anti-goat Alexa Fluor™ 647 secondary antibody (Invitrogen Cat#A-21447, 1:333) was used to identify the borders of the PPN. On an example slice to show the SNr injection site, sheep anti-TH primary antibody (Novus Biologicals Cat#NB300-110, 1:1000) and donkey anti-sheep (1:100) was used to delineate the GABAergic SNr from the dopamine-rich TH+ SNc neurons. To identify the approximate location of patched cells for cell mapping, slices were imaged as tiled z-stacks using a Leica SP8AOBS++ at the Microscopy and Imaging Shared Resource core facility at Georgetown University. Additionally, to verify the injection site and optical implant placement in the brain slices from mice that underwent behavioral testing, tiled z-stacks were obtained using either the aforementioned Leica SP8AOBS++ or a Zeiss Axio Imager Z2 at the Georgetown Department of Neuroscience core imaging facility.

Approximate Cell Location

An image of the PPN with the pipette tip still in position was taken at the end of each cell recording and confocal images of the slices after CUBIC clearing were obtained as described above. Confocal images were overlapped with the pipette images using the streptavidin-stained patched cells (which aligned with the pipette tip images) and autofluorescence of the superior cerebellar peduncle (scp) white fibers as landmarks. The perimeter of the PPN was determined by the presence of ChAT+ neurons and generally extended from the edge of the SNr to approximately 2/3 up the scp fibers. ChAT+ neurons were identified by tdTomato expression in the ChAT-Cre mouse line and anti-ChAT staining in the Vgat-Cre and Vglut2-Cre mouse lines. Slices were matched to their bregma reference in the Paxinos and Franklin's Mouse Brain Atlas 4th edition. Our sagittal slices were cut along the 1.00, 1.25, and 1.50-mm distance of the medial-lateral axis. All neurons on the most medial slice (1.00 mm) were considered 'caudal' and were aligned along the scp white fibers and edge of the slice. For slices 1.25 and 1.50 mm on the medial-lateral axis, the midline of cholinergic neuron distribution, which separates the loosely spread rostral neurons and densely packed caudal neurons, was aligned. The XY coordinates were determined using Fiji software and plotted in Igor. The color scale applied to the points represented the amplitude of the first oIPSC and ranged from 0 to 250pA so that amplitudes greater than 250pA were shown in the same maximal bright color.

Approximate Implant Location

To verify the location of the optical implant, anatomical landmarks for locating the PPN were identified by immunofluorescent labeled PPN cholinergic neurons. Sections containing visible optical fiber scarring were stained with anti-ChAT immunofluorescent labeling. These histological images were then visually matched to the corresponding sagittal planes of the stereotaxic atlas, based on the identified anatomical landmarks. The approximate position of the optical cannula was localized in the histological images.

QUANTIFICATION AND STATISTICAL ANALYSIS

Electrophysiological traces were processed in Igor Pro 9 (Wavemetrics) and all statistical analyses were performed in GraphPad Prism 9.5. For behavior experimental data, one-way ANOVA followed by Dunnett's post hoc test was performed. If the equality of variances was violated (i.e. the ratio of the largest and smallest standard deviations was greater than 2 and Barlett test was statistically significant), Welch's ANOVA test was alternatively used. For electrophysiological data, two-way ANOVA followed by Tukey's post hoc test was performed for percent of pre-optical stimulation frequency and two-tailed t-test was performed to compare the first oIPSC amplitude and PPR between rostral and caudal cholinergic neurons. All parametric data in text is reported as mean ± standard error of the mean (SEM). As the rest of the datasets did not follow a normal distribution, we used Mann-Whitney rank-sum test for comparing two groups and Kruskal-Wallis for multiple comparisons. As each comparison group within the Kruskal-Wallis tests was planned and stand alone, uncorrected Dunn's post hoc test was performed to determine significance between groups. Non-parametric data in text is reported as median [interquartile range (IQR)]. Boxplots show medians, 25th and 75th percentile as first and third quartile box edges, and 9th and 91st percentiles as whiskers. To determine if caudal GPe-connectivity is significantly greater than rostral

GPe-connectivity, as expected from axon projection patterns, a one-tailed Fisher's exact test and odds ratio effect size was performed. For correlation matrix analyses, non-parametric Spearman r was computed. Statistical details of experiments can be found in the text and figure legends. Biological replicates are individual cells (n) from 6 separate mice (N=3 males and 3 females) in the electrophysiological experiments and are individual mice of both sexes in the behavioral experiments (numbers described in results text). Same sex littermates were randomly allocated to control or experimental groups and experimenters were not blinded during experiments. Statistical significance was evaluated as $p < 0.05$.

Main figure titles and legends

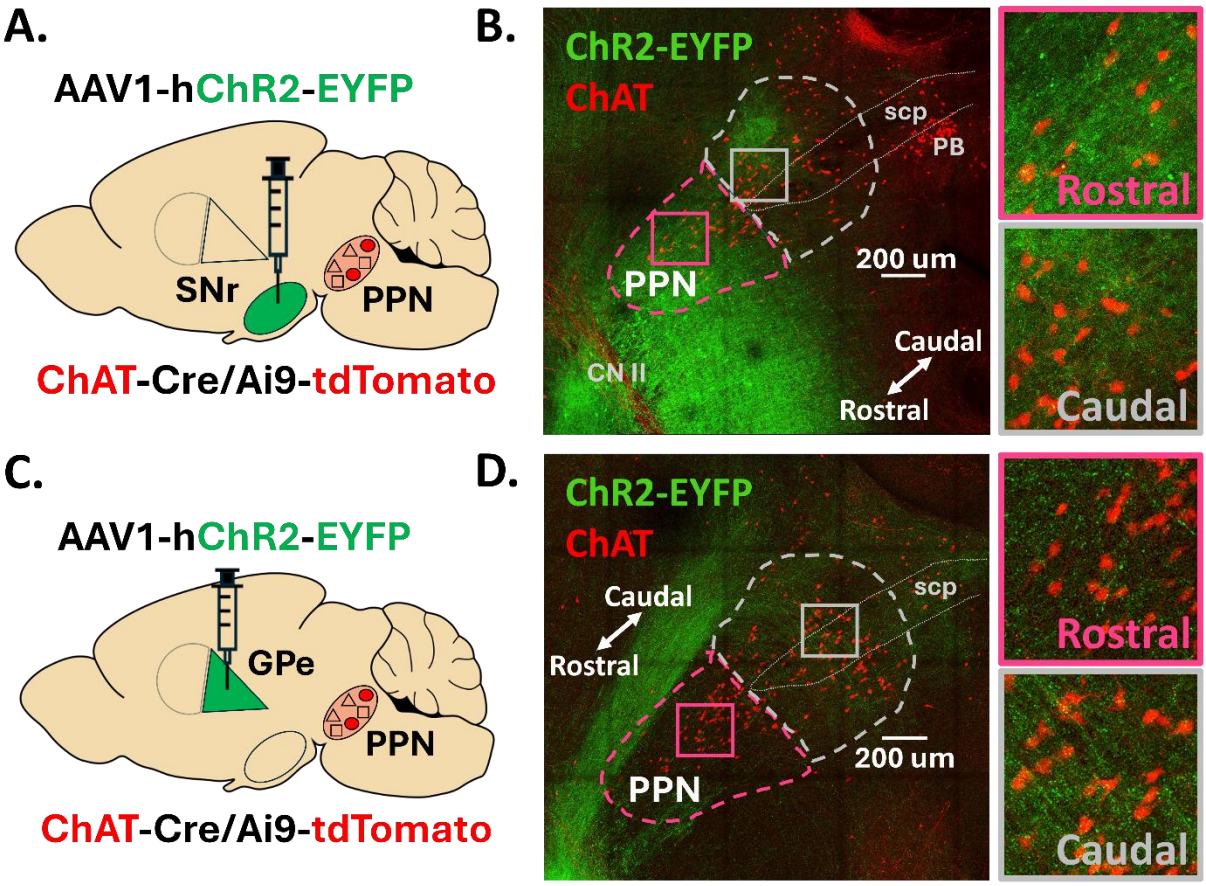

Figure 1. SNr and GPe axons display distinct distribution patterns across the rostral and caudal PPN. (A,C) Stereotaxic injection of AAV1 delivering *hSyn-ChR2-eYFP* to the SNr or GPe of ChAT-Cre/Ai9-tdTomato mice, respectively. (B, D) Confocal images of EYFP-filled SNr or GPe axons across the PPN, respectively. *CNII: cranial nerve II, scp: superior cerebellar peduncle; PB: parabrachial nucleus*

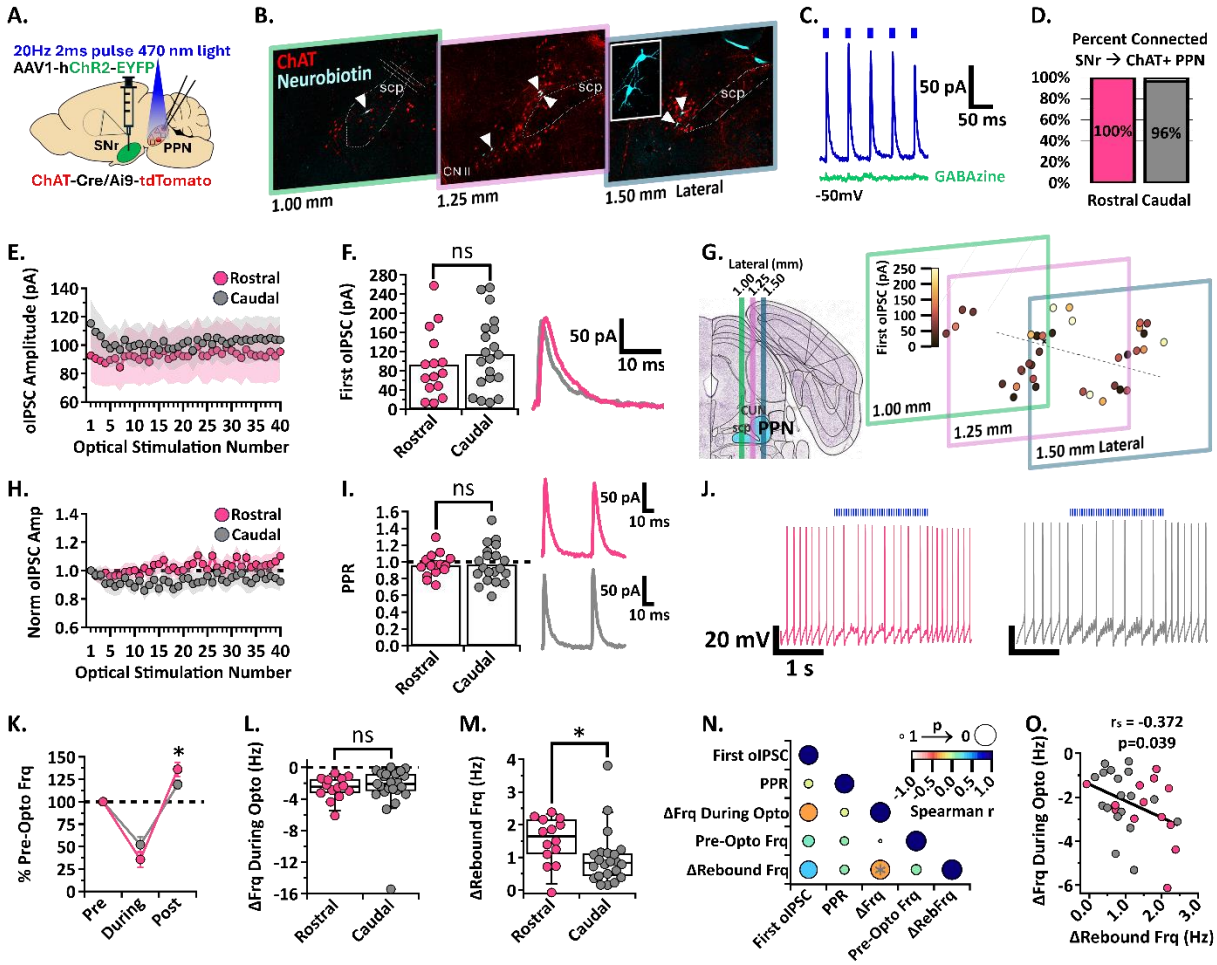

Figure 2. SNr inhibition of rostral and caudal ChAT+ PPN neurons. (A) Experimental set up to identify red ChAT+ PPN neurons for whole-cell patch clamp while stimulating ChR2-filled SNr axons [N=6]. (B) White arrowheads pointing to neurobiotin-filled patched neurons within the PPN across three 200µm slices. (C) Example trace of the first five oIPSCs [blue] in the 2-second 20 Hz train inhibited by GABA-a receptor blocker, GABAzine [green], while holding the cell at -50mV. (D) Percent connected among patched neurons in the rostral and caudal regions. (E) Average oIPSC amplitude at each of 40 optogenetic light pulses in n=15 rostral neurons and n=20 caudal neurons. (F) *Left*, Individual cell data for the first oIPSC amplitude and, *right*, example current traces. (G) Cell mapping of patched neuron locations with the first oIPSC amplitude represented by the color scale. (H) Normalized current amplitudes in E. (I) *Left*, Individual cell data for the PPR between the first two oIPSC amplitudes in the train and, *right*, example current traces. (J) Example voltage traces of action potential firing during a 2-second 20 Hz train stimulation in rostral (left) and caudal (right) neurons. (K) Percent of pre-optical stimulation firing frequency during stimulation and rebound in n=14 rostral vs n=23 caudal neurons; rebound rostral vs caudal p=0.0310. (L) Individual cell data for the absolute change in frequency during optical stimulation [ΔFrq During Opto]. (M) Individual cell data for the absolute change in rebound

frequency post-stimulation [ΔRebFrq]; rostral vs. caudal p=0.0142. (N) Correlation analysis, color scale representing Spearman r [-1,1] and size representing p-value [1,0]. (O) Negative correlation between the absolute change in frequency during stimulation and post-stimulation rebound; r=-0.372, p=0.039. * p<0.05; bar graph data represent mean ± SEM; box plots show median line with boxes showing IQR and whiskers showing 9th and 91st percentiles.

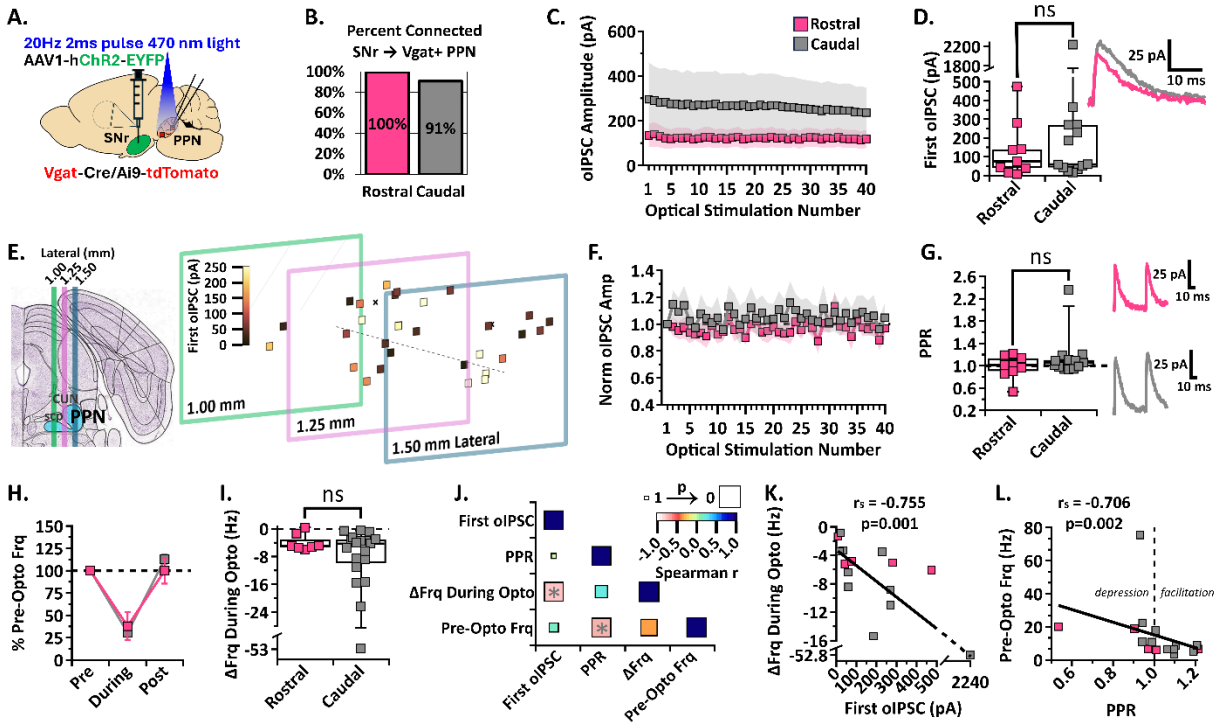

Figure 3. SNr inhibition of rostral and caudal Vgat+ PPN neurons. (A) Experimental set up to identify red Vgat+ PPN neurons for whole-cell patch clamp while stimulating ChR2-filled SNr axons [N=6]. (B) Percent connected among patched neurons in the rostral and caudal regions. (C) Average oIPSC amplitude at each of 40 optogenetic light pulses in n=9 rostral neurons and n=13 caudal neurons. (D) *Left*, Individual cell data for the first oIPSC amplitude and, *right*, example current traces. (E) Cell mapping of patched neuron locations with the first oIPSC amplitude represented by the color scale. (F) Normalized current amplitudes in C. (G) *Left*, Individual cell data for the PPR between the first two oIPSC amplitudes in the train and, *right*, example current traces. (H) Percent of pre-optical stimulation firing frequency [% Pre-Opto Frq] during stimulation and and rebound in n=7 rostral and n=19 caudal neurons. (I) Individual cell data for the absolute change in frequency during optical stimulation [ΔFrq During Opto]. (J) Correlation analysis, color scale representing Spearman r [-1,1] and size representing p-value [1,0]. (K) Negative correlation between the absolute change in frequency during stimulation and first oIPSC amplitude; r=-0.755, p=0.001. (L) Negative correlation between the pre-optical stimulation firing frequency and the PPR; r =-0.706, p=0.002. Box plots show median line with boxes showing IQR and whiskers showing 9th and 91st percentiles.

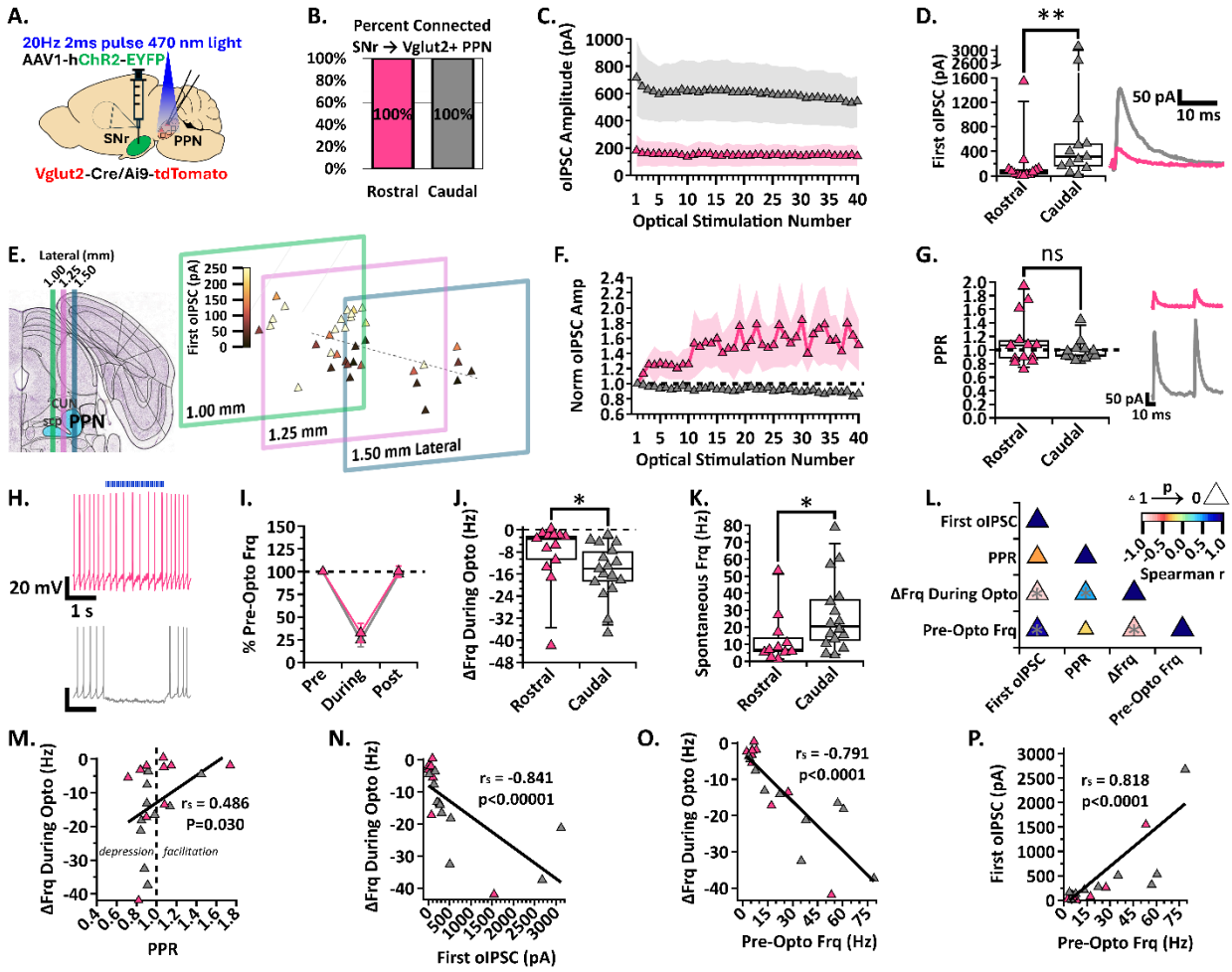

Figure 4. SNr inhibition of rostral and caudal Vglut2+ PPN neurons. (A) Experimental set up to identify red Vglut2+ PPN neurons for whole-cell patch clamp while stimulating ChR2-filled SNr axons [N=6]. (B) Percent connected among patched neurons in the rostral and caudal regions. (C) Average oIPSC amplitude at each of 40 optogenetic light pulses in n=13 rostral neurons and n=13 caudal neurons. (D) *Left*, Individual cell data for the first oIPSC amplitude and, *right*, example current traces; p=0.0035. (E) Cell mapping of patched locations with the first oIPSC amplitude represented by the color scale. (F) Normalized current amplitudes in C. (G) *Left*, Individual cell data for the PPR between the first two oIPSC amplitudes in the train and, *right*, example current traces. (H) Example voltage traces of action potential firing during a 2-second 20 Hz train stimulation in rostral and caudal neurons, top to bottom. (I) Percent of pre-optical stimulation firing frequency [% Pre-Opto Frq] during stimulation and rebound in n=13 rostral and n=17 caudal neurons. (J) Individual cell data for the absolute change in frequency during optical stimulation [ΔFrq During Opto]; p=0.0197. (K) Spontaneous frequency in n=11 rostral and n=16 caudal neurons; p=0.0343. (L) Correlation analysis, color scale representing Spearman r [-1,1] and size representing p-value [1,0]. (M) Positive correlation between the absolute change in frequency during stimulation and PPR, r=0.486, p=0.030. (N) Negative correlation between the absolute change in frequency during stimulation and first oIPSC amplitude; r=-0.841, p<0.00001. (O) Negative correlation between the absolute change in frequency during stimulation

and pre-optical stimulation frequency; r=-0.791, p<0.0001. (P) Positive correlation between the first oIPSC amplitude and pre-optical stimulation frequency; r=0.818, p<0.0001. * p<0.05, ** p<0.01; box plots show median line with boxes showing IQR and whiskers showing 9th and 91st percentiles.

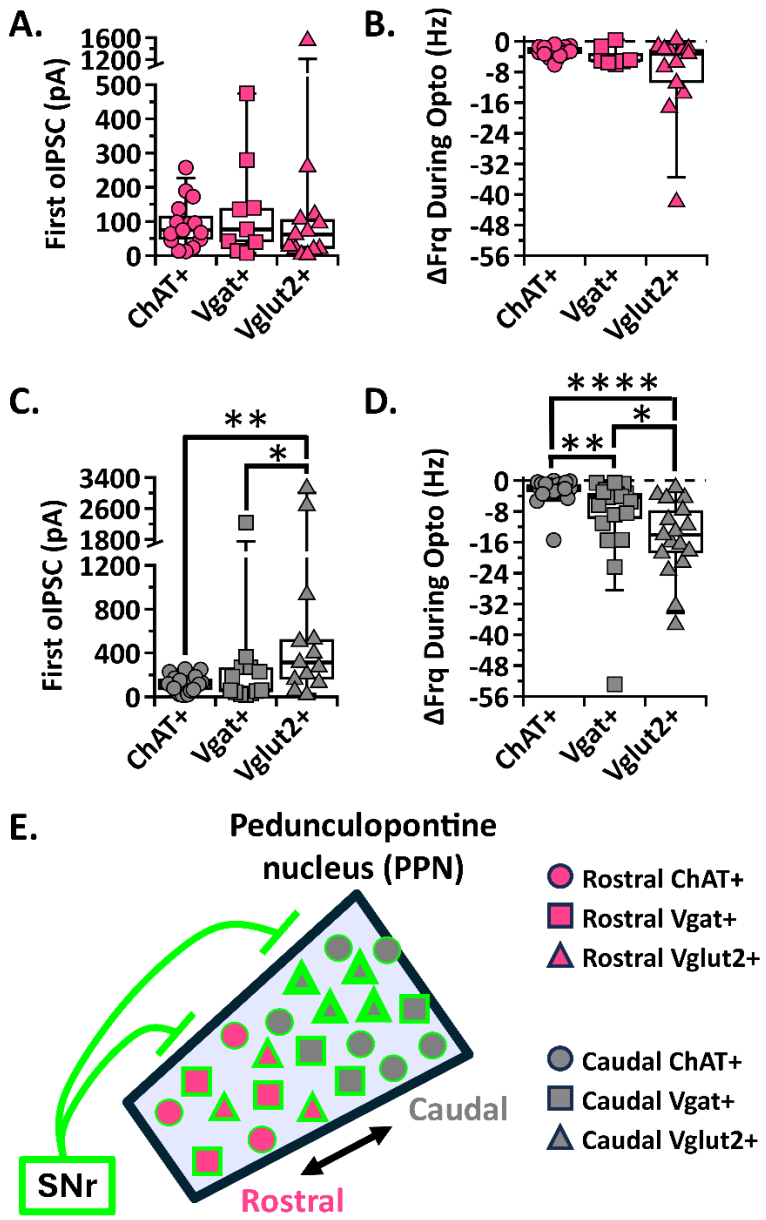

Figure 5. **The SNr most strongly inhibits caudal glutamatergic PPN neurons.** (A,C) Individual cell data for the first oIPSC amplitude recorded in each cell type for rostral and caudal PPN neurons, respectively. (B,D) Individual cell data for the absolute change in frequency during stimulation in each cell type for rostral and caudal PPN neurons, respectively. (E) Graphical depiction of SNr stimulation results. * $p<0.05$, ** $p<0.01$, **** $p<0.0001$; box plots show median line with boxes showing IQR and whiskers showing 9th and 91st percentiles.

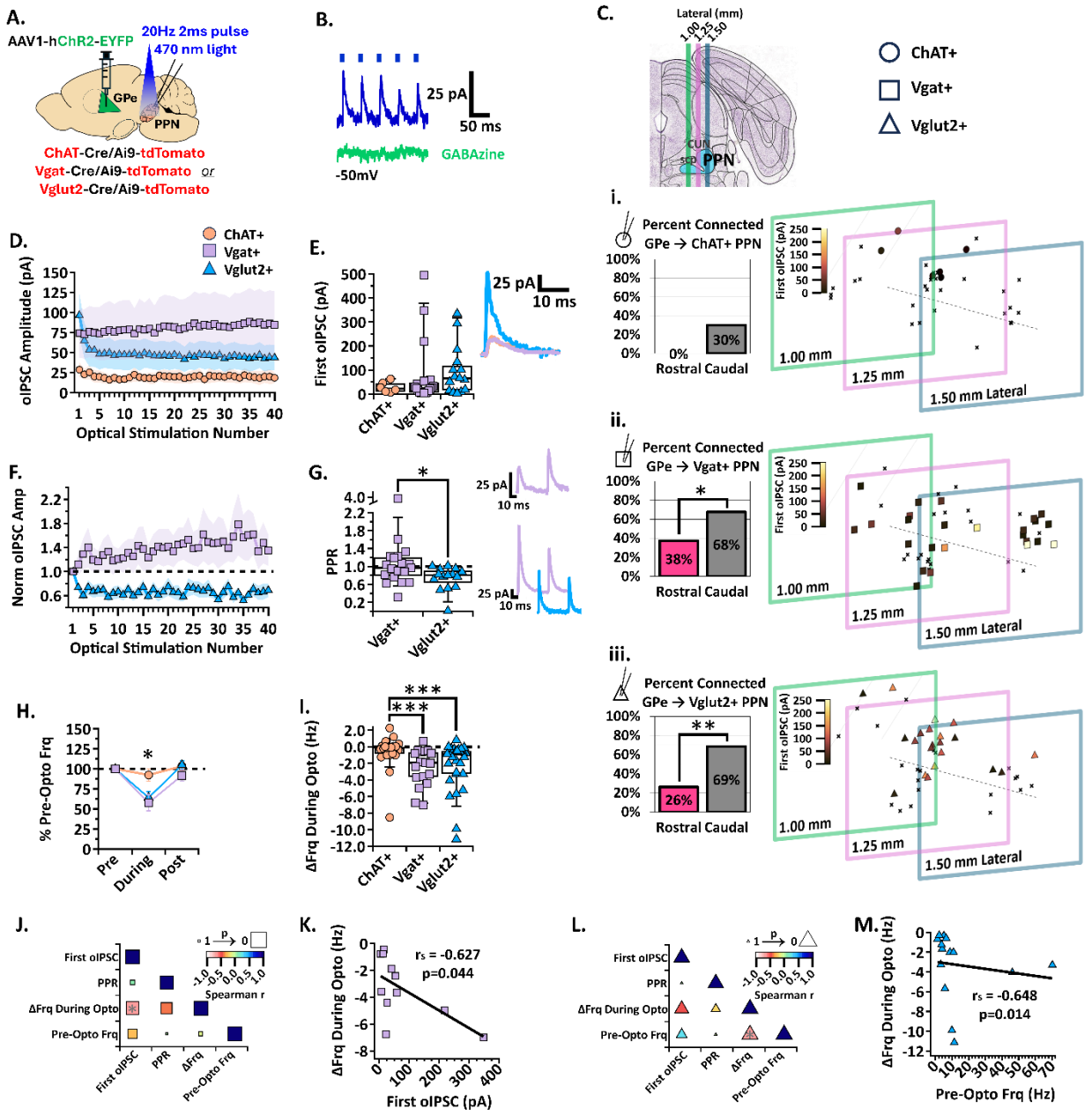

Figure 6. GPe inhibition of the three PPN cell types. (A) Experimental set up to identify red ChAT+, Vgat+, and Vglut2+ PPN neurons for whole-cell patch clamp while stimulating ChR2-filled GPe axons [N=6]. (B) Example trace of the first five oIPSCs in the 2-second 20 Hz train [blue] inhibited by GABA-a receptor blocker, GABAzine [green], while holding the cell at -50mV. (C) *Left*, Percent connected among patched neurons in the rostral and caudal regions and, *right*, cell mapping of patched locations with the first oIPSC amplitude represented by the color scale. *Top to bottom*, i. ChAT+, ii. Vgat+, and iii. Vglut2+ datasets. (D) Average oIPSC amplitude at each of 40 optogenetic light pulses in n=6 ChAT+, n=19 Vgat+, and n=15 Vglut2+ caudal PPN neurons. (E) *Left*, Individual cell data for the first oIPSC amplitude and, *right*, example current traces. (F) Normalized current amplitudes in C. (G) *Left*, Individual cell data for

the PPR between the first two oIPSC amplitudes in the train; p=0.0206. R*ight, top*, example current trace of short-term synaptic facilitation in VgAT+ neurons. *Right, bottom*, example current traces of short-term synaptic depression in Vgat+ and Vglut2+ neurons. (H) Percent of pre-optical stimulation firing frequency [%Pre-Opto Frq] during and post-stimulation in n=25 ChAT+, n=18 Vgat+, and n=29 Vglut2+ caudal PPN neurons. (I) Individual cell data for the absolute change in frequency during stimulation [ΔFrq During Opto]. (J) Correlation analysis for Vgat+ neurons, color scale representing Spearman r [-1,1] and size representing p-value [1,0]. (K) Negative correlation between the absolute change in frequency during stimulation and first oIPSC amplitude; r=-0.627, p=0.044. (L) Correlation analysis for Vglut2+ neurons. (M) Negative correlation between the absolute change in frequency during stimulation and the pre-stimulation firing frequency; r=-0.648, p=0.014. *p<0.05, **p<0.01; box plots show median line with boxes showing IQR and whiskers showing 9th and 91st percentiles.

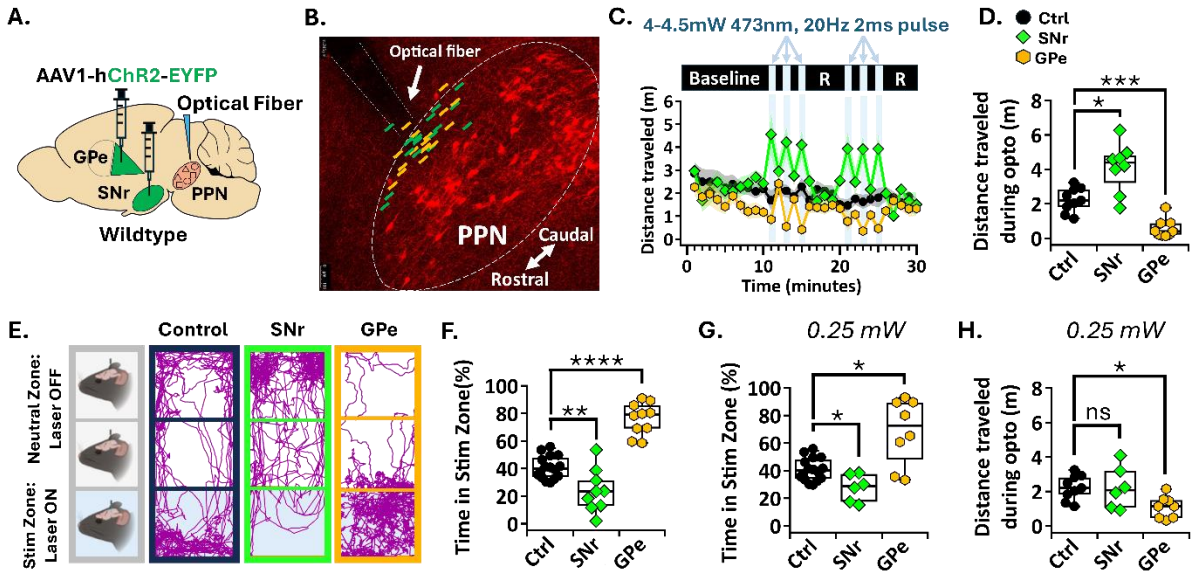

***Figure 7. In vivo* activation of GPe and SNr axons in the PPN show opposite effects on locomotion and valence.** (A) Experimental set up to stimulate ChR2-filled SNr or GPe axons over the PPN in vivo. (B) Representative image of optical fiber tract overlaid with the approximate optical fiber placement for SNr- [green] and GPe- [orange] injected mice. (C) Distance traveled over time in an open field with 1 minute 20 Hz optical stimulations over the PPN in N=9 control (Ctrl) mice (black circles), N=8 mice injected with ChR2 in the SNr (green diamonds), and N=9 mice injected with ChR2 in the GPe (orange hexagons); R=recovery period. (D) Average distance traveled for each mouse across the six 1minute optical stimulations. (E) Representative mouse track tracings during real time place preference task in a three-chamber box and continuously stimulating EGFP- or ChR2-filled axons over the PPN at 20 Hz in SNr- and GPe-injected mice when the mice are in the stimulation zone. (F) Percent time spent in the stimulation zone in N=16 control mice, N=9 mice injected with ChR2 in the SNr, and N=10 mice injected with ChR2 in the GPe. (G) Average distance traveled in the open field during optical stimulations and (H) percent time spent in the stimulation zone using 0.25 mW laser power in N=6 mice injected with ChR2 in the SNr and N=8 mice injected with ChR2 in the GPe. * p<0.05, ** p<0.01, *** p<0.001, **** p<0.0001; box plots show median line with boxes showing IQR and whiskers showing 9th and 91st percentiles. See related supplemental Video S1-S4.

Supplemental information

Document S1. Figure S1, related to Figures 2, 3, 4, & 6

Video S1. Example video of stimulating SNr axons over the PPN in an open field, related to Figure 7

Video S2. Example video of stimulating GPe axons over the PPN in an open field, related to Figure 7

Video S3. Example video of stimulating SNr axons over the PPN in the striped zone, related to Figure 7

Video S4. Example video of stimulating GPe axons over the PPN in the striped zone, related to Figure 7

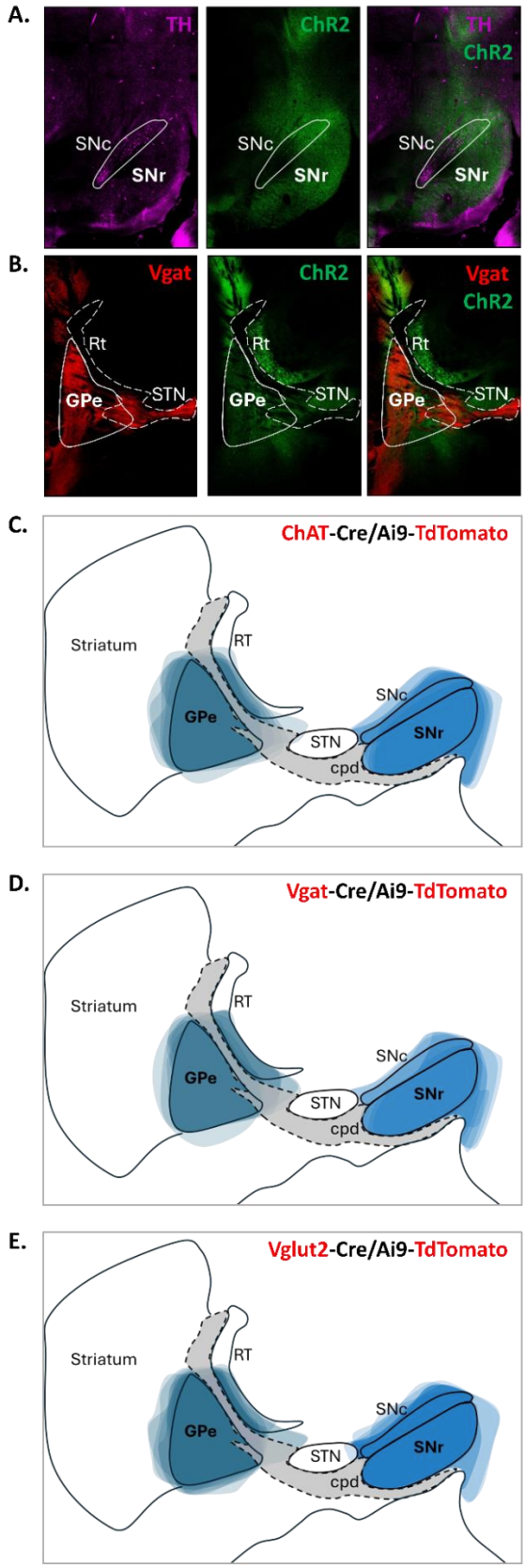

1163

Figure S1. (A) Representative image of SNr injected with ChR2-EYFP. Cell bodies and axons filled with ChR2 are represented in green. Post hoc staining of tyrosine hydroxylase (TH) to label dopamine neurons in the substantia nigra *pars compacta*. TH+ neurons are represented in magenta. **(B)** Representative image of GPe injected with ChR2-EYFP in a Vgat-Cre/Ai9-TdTomato mouse. Cell bodies and axons filled with ChR2 are represented in green. Vgat+ neurons and their axonal projections are represented in red. **(C-E)** Graphical depiction of virus spread in N=6 SNr and N=6 GPe injected mice in each mouse line: **(C)** ChAT-Cre/Ai9-TdTomato, **(D)** Vgat-Cre/Ai9-TdTomato, and **(E)** Vglut2-Cre/Ai9-TdTomato mice.

References

1. Ryczko, D. (2022). The Mesencephalic Locomotor Region: Multiple Cell Types, Multiple Behavioral Roles, and Multiple Implications for Disease. Neuroscientist, 10738584221139136. https://doi.org/10.1177/10738584221139136.
2. Bastos-Gonçalves, R., Coimbra, B., and Rodrigues, A.J. (2024). The mesopontine tegmentum in reward and aversion: from cellular heterogeneity to behaviour. Neuroscience & Biobehavioral Reviews, 105702. https://doi.org/10.1016/j.neubiorev.2024.105702.
3. Mena-Segovia, J., and Bolam, J.P. (2017). Rethinking the Pedunculopontine Nucleus: From Cellular Organization to Function. Neuron *94*, 7–18. https://doi.org/10.1016/j.neuron.2017.02.027.
4. French, I.T., and Muthusamy, K.A. (2018). A Review of the Pedunculopontine Nucleus in Parkinson's Disease. Frontiers in Aging Neuroscience *10*, 99. https://doi.org/10.3389/fnagi.2018.00099.
5. Wang, H.-L., and Morales, M. (2009). Pedunculopontine and laterodorsal tegmental nuclei contain distinct populations of cholinergic, glutamatergic and GABAergic neurons in the rat. Eur J Neurosci *29*, 10.1111/j.1460-9568.2008.06576.x. https://doi.org/10.1111/j.1460-9568.2008.06576.x.
6. Mena-Segovia, J., Micklem, B. r., Nair-Roberts, R. g., Ungless, M. a., and Bolam, J. p. (2009). GABAergic neuron distribution in the pedunculopontine nucleus defines functional subterritories. Journal of Comparative Neurology *515*, 397–408. https://doi.org/10.1002/cne.22065.
7. Yoo, J.H., Zell, V., Wu, J., Punta, C., Ramajayam, N., Shen, X., Faget, L., Lilascharoen, V., Lim, B.K., and Hnasko, T.S. (2017). Activation of Pedunculopontine Glutamate Neurons Is Reinforcing. J Neurosci *37*, 38–46. https://doi.org/10.1523/JNEUROSCI.3082-16.2016.
8. Steinkellner, T., Yoo, J.H., and Hnasko, T.S. (2019). Differential Expression of VGLUT2 in Mouse Mesopontine Cholinergic Neurons. eNeuro *6*. https://doi.org/10.1523/ENEURO.0161-19.2019.
9. Martinez-Gonzalez, C., Bolam, J., and Mena-Segovia, J. (2011). Topographical Organization of the Pedunculopontine Nucleus. Frontiers in Neuroanatomy *5*, 22. https://doi.org/10.3389/fnana.2011.00022.
10. Alam, M., Schwabe, K., and Krauss, J.K. (2011). The pedunculopontine nucleus area: critical evaluation of interspecies differences relevant for its use as a target for deep brain stimulation. Brain *134*, 11–23. https://doi.org/10.1093/brain/awq322.
11. Marín, O., Smeets, W.J.A.J., and González, A. (1998). Evolution of the basal ganglia in tetrapods: a new perspective based on recent studies in amphibians.

Trends in Neurosciences *21*, 487–494. https://doi.org/10.1016/S0166-2236(98)01297-1.

12. McElvain, L.E., Chen, Y., Moore, J.D., Brigidi, G.S., Bloodgood, B.L., Lim, B.K., Costa, R.M., and Kleinfeld, D. (2021). Specific populations of basal ganglia output neurons target distinct brain stem areas while collateralizing throughout the diencephalon. Neuron *109*, 1721-1738.e4. https://doi.org/10.1016/j.neuron.2021.03.017.
13. Zhao, P., Wang, H., Li, A., Sun, Q., Jiang, T., Li, X., and Gong, H. (2022). The Mesoscopic Connectome of the Cholinergic Pontomesencephalic Tegmentum. Frontiers in Neuroanatomy 16:843303. https://doi.org/10.3389/fnana.2022.843303
14. Roseberry, T.K., Lee, A.M., Lalive, A.L., Wilbrecht, L., Bonci, A., and Kreitzer, A.C. (2016). Cell-Type-Specific Control of Brainstem Locomotor Circuits by Basal Ganglia. Cell *164*, 526–537. https://doi.org/10.1016/j.cell.2015.12.037.
15. Huerta-Ocampo, I., Dautan, D., Gut, N.K., Khan, B., and Mena-Segovia, J. (2021). Whole-brain mapping of monosynaptic inputs to midbrain cholinergic neurons. Sci Rep *11*, 9055. https://doi.org/10.1038/s41598-021-88374-6.
16. Dautan, D., Kovács, A., Bayasgalan, T., Diaz-Acevedo, M.A., Pal, B., and Mena-Segovia, J. (2021). Modulation of motor behavior by the mesencephalic locomotor region. Cell Reports *36*. https://doi.org/10.1016/j.celrep.2021.109594.
17. Caggiano, V., Leiras, R., Goñi-Erro, H., Masini, D., Bellardita, C., Bouvier, J., Caldeira, V., Fisone, G., and Kiehn, O. (2018). Midbrain circuits that set locomotor speed and gait selection. Nature *553*, 455–460. https://doi.org/10.1038/nature25448.
18. Henrich, M.T., Geibl, F.F., Lakshminarasimhan, H., Stegmann, A., Giasson, B.I., Mao, X., Dawson, V.L., Dawson, T.M., Oertel, W.H., and Surmeier, D.J. (2020). Determinants of seeding and spreading of α-synuclein pathology in the brain. Sci Adv *6*. https://doi.org/10.1126/sciadv.abc2487.
19. Ugolini, G. (2011). Chapter 10 - Rabies Virus as a Transneuronal Tracer of Neuronal Connections. In Advances in Virus Research Research Advances in Rabies., A. C. Jackson, ed. (Academic Press), pp. 165–202. https://doi.org/10.1016/B978-0-12-387040-7.00010-X.
20. Linders, L.E., Supiot, Laura.F., Du, W., D'Angelo, R., Adan, R.A.H., Riga, D., and Meye, F.J. (2022). Studying Synaptic Connectivity and Strength with Optogenetics and Patch-Clamp Electrophysiology. Int J Mol Sci *23*, 11612. https://doi.org/10.3390/ijms231911612.
21. Glasgow, S.D., McPhedrain, R., Madranges, J.F., Kennedy, T.E., and Ruthazer, E.S. (2019). Approaches and Limitations in the Investigation of Synaptic Transmission and Plasticity. Front. Synaptic Neurosci. *11*. https://doi.org/10.3389/fnsyn.2019.00020.
22. Goñi-Erro, H., Selvan, R., Leiras, R., and Kiehn, O. (2023). Pedunculopontine Chx10+ neurons control global motor arrest in mice. Nat Neurosci, 1–13. https://doi.org/10.1038/s41593-023-01396-3.
23. Masini, D., and Kiehn, O. (2022). Targeted activation of midbrain neurons restores locomotor function in mouse models of parkinsonism. Nat Commun *13*, 504. https://doi.org/10.1038/s41467-022-28075-4.

24. Gut, N.K., Yilmaz, D., Kondabolu, K., Huerta-Ocampo, I., and Mena-Segovia, J. (2022). Selective inhibition of goal-directed actions in the mesencephalic locomotor region (Neuroscience) https://doi.org/10.1101/2022.01.18.476772.
25. Josset, N., Roussel, M., Lemieux, M., Lafrance-Zoubga, D., Rastqar, A., and Bretzner, F. (2018). Distinct Contributions of Mesencephalic Locomotor Region Nuclei to Locomotor Control in the Freely Behaving Mouse. Current Biology *28*, 884-901.e3. https://doi.org/10.1016/j.cub.2018.02.007.
26. Tello, A.J., Zouwen, C.I. van der, Dejas, L., Duque-Yate, J., Boutin, J., Medina-Ortiz, K., Suresh, J.S., Swiegers, J., Sarret, P., and Ryczko, D. (2024). Dopamine-sensitive neurons in the mesencephalic locomotor region control locomotion initiation, stop, and turns. Cell Reports *43*. https://doi.org/10.1016/j.celrep.2024.114187.
27. Xiao, C., Cho, J.R., Zhou, C., Treweek, J.B., Chan, K., McKinney, S.L., Yang, B., and Gradinaru, V. (2016). Cholinergic Mesopontine Signals Govern Locomotion and Reward through Dissociable Midbrain Pathways. Neuron *90*, 333–347. https://doi.org/10.1016/j.neuron.2016.03.028.
28. Dautan, D., Souza, A.S., Huerta-Ocampo, I., Valencia, M., Assous, M., Witten, I.B., Deisseroth, K., Tepper, J.M., Bolam, J.P., Gerdjikov, T.V., et al. (2016). Segregated cholinergic transmission modulates dopamine neurons integrated in distinct functional circuits. Nat Neurosci *19*, 1025–1033. https://doi.org/10.1038/nn.4335.
29. Ferreira-Pinto, M.J., Kanodia, H., Falasconi, A., Sigrist, M., Esposito, M.S., and Arber, S. (2021). Functional diversity for body actions in the mesencephalic locomotor region. Cell *184*, 4564-4578.e18. https://doi.org/10.1016/j.cell.2021.07.002.
30. Zhang, S., Mena-Segovia, J., and Gut, N.K. (2024). Inhibitory Pedunculopontine Neurons Gate Dopamine-Mediated Motor Actions of Unsigned Valence. Curr Neuropharmacol *22*, 1540–1550. https://doi.org/10.2174/1570159X21666230911103520.
31. Hormigo, S., Vega-Flores, G., Rovira, V., and Castro-Alamancos, M.A. (2019). Circuits That Mediate Expression of Signaled Active Avoidance Converge in the Pedunculopontine Tegmentum. J. Neurosci. *39*, 4576–4594. https://doi.org/10.1523/JNEUROSCI.0049-19.2019.
32. Hormigo, S., Shanmugasundaram, B., Zhou, J., and Castro-Alamancos, M.A. (2021). A Signaled Locomotor Avoidance Action Is Fully Represented in the Neural Activity of the Midbrain Tegmentum. J. Neurosci. *41*, 4262–4275. https://doi.org/10.1523/JNEUROSCI.0027-21.2021.
33. Rizzi, G., and Tan, K.R. (2019). Synergistic Nigral Output Pathways Shape Movement. Cell Reports *27*, 2184-2198.e4. https://doi.org/10.1016/j.celrep.2019.04.068.
34. Liu, A., Cheng, Y., and Huang, J. (2023). Neurons innervating both the central amygdala and the ventral tegmental area encode different emotional valences. Front Neurosci *17*, 1178693. https://doi.org/10.3389/fnins.2023.1178693.
35. Galaj, E., Han, X., Shen, H., Jordan, C.J., He, Y., Humburg, B., Bi, G.-H., and Xi, Z.-X. (2020). Dissecting the Role of GABA Neurons in the VTA versus SNr in Opioid Reward. J Neurosci *40*, 8853–8869. https://doi.org/10.1523/JNEUROSCI.0988-20.2020.

36. Mastro, K.J., Bouchard, R.S., Holt, H.A.K., and Gittis, A.H. (2014). Transgenic Mouse Lines Subdivide External Segment of the Globus Pallidus (GPe) Neurons and Reveal Distinct GPe Output Pathways. J. Neurosci. *34*, 2087–2099. https://doi.org/10.1523/JNEUROSCI.4646-13.2014.
37. Tian, J., Yan, Y., Xi, W., Zhou, R., Lou, H., Duan, S., Chen, J.F., and Zhang, B. (2018). Optogenetic Stimulation of GABAergic Neurons in the Globus Pallidus Produces Hyperkinesia. Front Behav Neurosci *12*, 185. https://doi.org/10.3389/fnbeh.2018.00185.
38. Pamukcu, A., Cui, Q., Xenias, H.S., Berceau, B.L., Augustine, E.C., Fan, I., Chalasani, S., Hantman, A.W., Lerner, T.N., Boca, S.M., et al. (2020). Parvalbumin+ and Npas1+ Pallidal Neurons Have Distinct Circuit Topology and Function. J Neurosci *40*, 7855–7876. https://doi.org/10.1523/JNEUROSCI.0361-20.2020.
39. Cui, Q., Pamukcu, A., Cherian, S., Chang, I.Y.M., Berceau, B.L., Xenias, H.S., Higgs, M.H., Rajamanickam, S., Chen, Y., Du, X., et al. (2021). Dissociable Roles of Pallidal Neuron Subtypes in Regulating Motor Patterns. J. Neurosci. *41*, 4036–4059. https://doi.org/10.1523/JNEUROSCI.2210-20.2021.
40. Aristieta, A., Barresi, M., Azizpour Lindi, S., Barrière, G., Courtand, G., de la Crompe, B., Guilhemsang, L., Gauthier, S., Fioramonti, S., Baufreton, J., et al. (2021). A Disynaptic Circuit in the Globus Pallidus Controls Locomotion Inhibition. Current Biology *31*, 707-721.e7. https://doi.org/10.1016/j.cub.2020.11.019.
41. Isett, B.R., Nguyen, K.P., Schwenk, J.C., Yurek, J.R., Snyder, C.N., Vounatsos, M.V., Adegbesan, K.A., Ziausyte, U., and Gittis, A.H. (2023). The indirect pathway of the basal ganglia promotes transient punishment but not motor suppression. Neuron. https://doi.org/10.1016/j.neuron.2023.04.017.
42. Susaki, E.A., Tainaka, K., Perrin, D., Yukinaga, H., Kuno, A., and Ueda, H.R. (2015). Advanced CUBIC protocols for whole-brain and whole-body clearing and imaging. Nat Protoc *10*, 1709–1727. https://doi.org/10.1038/nprot.2015.085.
43. Ambrosi, P., and Lerner, T.N. (2022). Striatonigrostriatal circuit architecture for disinhibition of dopamine signaling. Cell Reports *40*. https://doi.org/10.1016/j.celrep.2022.111228.
44. Buchholz, M.O., Guilabert, A.G., Ehret, B., and Schuhknecht, G.F.P. (2023). How synaptic strength, short-term plasticity, and input synchrony contribute to neuronal spike output. PLOS Computational Biology *19*, e1011046. https://doi.org/10.1371/journal.pcbi.1011046.
45. Chen, R.Y.-T., and Evans, R.C. (2024). Comparing tonic and phasic dendritic calcium in cholinergic pedunculopontine neurons and dopaminergic substantia nigra neurons. European Journal of Neuroscience *59*, 1638–1656. https://doi.org/10.1111/ejn.16281.
46. Tubert, C., Zampese, E., Pancani, T., Tkatch, T., and Surmeier, D.J. (2023). Feed-forward metabotropic signaling by Cav1 Ca2+ channels supports pacemaking in pedunculopontine cholinergic neurons. Neurobiology of Disease *188*, 106328. https://doi.org/10.1016/j.nbd.2023.106328.
47. Takakusaki, K., Shiroyama, T., and Kitai, S.T. (1997). Two types of cholinergic neurons in the rat tegmental pedunculopontine nucleus: electrophysiological and morphological characterization. Neuroscience *79*, 1089–1109. https://doi.org/10.1016/S0306-4522(97)00019-5.

48. Baksa, B., Kovács, A., Bayasgalan, T., Szentesi, P., Kőszeghy, Á., Szücs, P., and Pál, B. (2019). Characterization of functional subgroups among genetically identified cholinergic neurons in the pedunculopontine nucleus. Cell. Mol. Life Sci. *76*, 2799–2815. https://doi.org/10.1007/s00018-019-03025-4.
49. Kroeger, D., Ferrari, L.L., Petit, G., Mahoney, C.E., Fuller, P.M., Arrigoni, E., and Scammell, T.E. (2017). Cholinergic, Glutamatergic, and GABAergic Neurons of the Pedunculopontine Tegmental Nucleus Have Distinct Effects on Sleep/Wake Behavior in Mice. J Neurosci *37*, 1352–1366. https://doi.org/10.1523/JNEUROSCI.1405-16.2016.
50. Granata, A.R., and Kitai, S.T. (1991). Inhibitory substantia nigra inputs to the pedunculopontine neurons. Exp Brain Res *86*, 459–466. https://doi.org/10.1007/BF00230520.
51. Kang, Y., and Kitai, S.T. (1990). Electrophysiological properties of pedunculopontine neurons and their postsynaptic responses following stimulation of substantia nigra reticulata. Brain Research *535*, 79–95. https://doi.org/10.1016/0006-8993(90)91826-3.
52. Evans, R.C., Zhu, M., and Khaliq, Z.M. (2017). Dopamine Inhibition Differentially Controls Excitability of Substantia Nigra Dopamine Neuron Subpopulations through T-Type Calcium Channels. J. Neurosci. *37*, 3704–3720. https://doi.org/10.1523/JNEUROSCI.0117-17.2017.
53. Villalobos, C.A., and Basso, M.A. (2022). Optogenetic activation of the inhibitory nigro-collicular circuit evokes contralateral orienting movements in mice. Cell Rep *39*, 110699. https://doi.org/10.1016/j.celrep.2022.110699.
54. Rajaram, E., Kaltenbach, C., Fischl, M.J., Mrowka, L., Alexandrova, O., Grothe, B., Hennig, M.H., and Kopp-Scheinpflug, C. (2019). Slow NMDA-Mediated Excitation Accelerates Offset-Response Latencies Generated via a Post-Inhibitory Rebound Mechanism. eNeuro *6*. https://doi.org/10.1523/ENEURO.0106-19.2019.
55. Zhu, T., Wei, S., and Wang, Y. (2022). Post-Inhibitory Rebound Firing of Dorsal Root Ganglia Neurons. J Pain Res *15*, 2029–2040. https://doi.org/10.2147/JPR.S370335.
56. Sivaramakrishnan, S., and Lynch, W.P. (2017). Rebound from Inhibition: Self-Correction against Neurodegeneration? J Clin Cell Immunol *8*, 492. https://doi.org/10.4172/2155-9899.1000492.
57. Bordas, C., Kovacs, A., and Pal, B. (2015). The M-current contributes to high threshold membrane potential oscillations in a cell type-specific way in the pedunculopontine nucleus of mice. Frontiers in Cellular Neuroscience *9*:121. https://doi.org/10.3389/fncel.2015.00121.
58. Aitta-aho, T., Hay, Y.A., Phillips, B.U., Saksida, L.M., Bussey, T.J., Paulsen, O., and Apergis-Schoute, J. (2018). Basal Forebrain and Brainstem Cholinergic Neurons Differentially Impact Amygdala Circuits and Learning-Related Behavior. Current Biology *28*, 2557-2569.e4. https://doi.org/10.1016/j.cub.2018.06.064.
59. Dong, J., Hawes, S., Wu, J., Le, W., and Cai, H. (2021). Connectivity and Functionality of the Globus Pallidus Externa Under Normal Conditions and Parkinson's Disease. Frontiers in Neural Circuits *15*:645287. https://doi.org/10.3389/fncir.2021.645287.

60. Lilascharoen, V., Wang, E.H.-J., Do, N., Pate, S.C., Tran, A.N., Yoon, C.D., Choi, J.-H., Wang, X.-Y., Pribiag, H., Park, Y.-G., et al. (2021). Divergent pallidal pathways underlying distinct Parkinsonian behavioral deficits. Nat Neurosci *24*, 504–515. https://doi.org/10.1038/s41593-021-00810-y.
61. Barter, J.W., Li, S., Sukharnikova, T., Rossi, M.A., Bartholomew, R.A., and Yin, H.H. (2015). Basal Ganglia Outputs Map Instantaneous Position Coordinates during Behavior. J. Neurosci. *35*, 2703–2716. https://doi.org/10.1523/JNEUROSCI.3245-14.2015.
62. Gulley, J.M., Kuwajima, M., Mayhill, E., and Rebec, G.V. (1999). Behavior-related changes in the activity of substantia nigra pars reticulata neurons in freely moving rats. Brain Research *845*, 68–76. https://doi.org/10.1016/S0006-8993(99)01932-0.
63. Liu, D., Li, W., Ma, C., Zheng, W., Yao, Y., Tso, C.F., Zhong, P., Chen, X., Song, J.H., Choi, W., et al. (2020). A common hub for sleep and motor control in the substantia nigra. Science *367*, 440–445. https://doi.org/10.1126/science.aaz0956.
64. Meyer-Luehmann, M., Thompson, J.F., Berridge, K.C., and Aldridge, J.W. (2002). Substantia nigra pars reticulata neurons code initiation of a serial pattern: implications for natural action sequences and sequential disorders. European Journal of Neuroscience *16*, 1599–1608. https://doi.org/10.1046/j.1460-9568.2002.02210.x.
65. Dodson, P.D., Larvin, J.T., Duffell, J.M., Garas, F.N., Doig, N.M., Kessaris, N., Duguid, I.C., Bogacz, R., Butt, S.J.B., and Magill, P.J. (2015). Distinct developmental origins manifest in the specialized encoding of movement by adult neurons of the external globus pallidus. Neuron *86*, 501–513. https://doi.org/10.1016/j.neuron.2015.03.007.
66. Turner, R.S., and Anderson, M.E. (1997). Pallidal Discharge Related to the Kinematics of Reaching Movements in Two Dimensions. Journal of Neurophysiology *77*, 1051–1074. https://doi.org/10.1152/jn.1997.77.3.1051.
67. Schultz, W. (1986). Activity of pars reticulata neurons of monkey substantia nigra in relation to motor, sensory, and complex events. J Neurophysiol *55*, 660–677. https://doi.org/10.1152/jn.1986.55.4.660.
68. Freeze, B.S., Kravitz, A.V., Hammack, N., Berke, J.D., and Kreitzer, A.C. (2013). Control of Basal Ganglia Output by Direct and Indirect Pathway Projection Neurons. J Neurosci *33*, 18531–18539. https://doi.org/10.1523/JNEUROSCI.1278-13.2013.
69. Deniau, J.M., Kitai, S.T., Donoghue, J.P., and Grofova, I. (1982). Neuronal interactions in the substantia nigra pars reticulata through axon collaterals of the projection neurons. An electrophysiological and morphological study. Exp Brain Res *47*, 105–113. https://doi.org/10.1007/BF00235891.
70. Mailly, P., Charpier, S., Menetrey, A., and Deniau, J.-M. (2003). Three-Dimensional Organization of the Recurrent Axon Collateral Network of the Substantia Nigra Pars Reticulata Neurons in the Rat. J. Neurosci. *23*, 5247–5257. https://doi.org/10.1523/JNEUROSCI.23-12-05247.2003.
71. Mastro, K.J., Zitelli, K.T., Willard, A.M., Leblanc, K.H., Kravitz, A.V., and Gittis, A.H. (2017). Cell-specific pallidal intervention induces long-lasting motor recovery in dopamine-depleted mice. Nat Neurosci *20*, 815–823. https://doi.org/10.1038/nn.4559.

72. Kita, H., and Kita, S.T. (1994). The morphology of globus pallidus projection neurons in the rat: an intracellular staining study. Brain Research *636*, 308–319. https://doi.org/10.1016/0006-8993(94)91030-8.
73. Sadek, A.R., Magill, P.J., and Bolam, J.P. (2007). A Single-Cell Analysis of Intrinsic Connectivity in the Rat Globus Pallidus. J. Neurosci. *27*, 6352–6362. https://doi.org/10.1523/JNEUROSCI.0953-07.2007.
74. Ryczko, D., Cone, J.J., Alpert, M.H., and Dubuc, R. (2016). A descending dopamine pathway conserved from basal vertebrates to mammals. PNAS *113*. https://doi.org/10.1073/pnas.1600684113.
75. Kravitz, A.V., Freeze, B.S., Parker, P.R.L., Kay, K., Thwin, M.T., Deisseroth, K., and Kreitzer, A.C. (2010). Regulation of parkinsonian motor behaviours by optogenetic control of basal ganglia circuitry. Nature *466*, 622–626. https://doi.org/10.1038/nature09159.
76. Baker, M., Kang, S., Hong, S.-I., Song, M., Yang, M.A., Peyton, L., Essa, H., Lee, S.W., and Choi, D.-S. (2023). External globus pallidus input to the dorsal striatum regulates habitual seeking behavior in male mice. Nat Commun *14*, 4085. https://doi.org/10.1038/s41467-023-39545-8.
77. Farries, M.A., Faust, T.W., Mohebi, A., and Berke, J.D. (2023). Selective encoding of reward predictions and prediction errors by globus pallidus subpopulations. Current Biology *0*. https://doi.org/10.1016/j.cub.2023.08.042.
78. Arkadir, D., Morris, G., Vaadia, E., and Bergman, H. (2004). Independent Coding of Movement Direction and Reward Prediction by Single Pallidal Neurons. J. Neurosci. *24*, 10047–10056. https://doi.org/10.1523/JNEUROSCI.2583-04.2004.
79. Forster, G.L., and Blaha, C.D. (2003). Pedunculopontine tegmental stimulation evokes striatal dopamine efflux by activation of acetylcholine and glutamate receptors in the midbrain and pons of the rat. Eur J Neurosci *17*, 751–762. https://doi.org/10.1046/j.1460-9568.2003.02511.x.
80. Estakhr, J., Abazari, D., Frisby, K., McIntosh, J.M., and Nashmi, R. (2017). Differential Control of Dopaminergic Excitability and Locomotion by Cholinergic Inputs in Mouse Substantia Nigra. Current Biology *27*, 1900-1914.e4. https://doi.org/10.1016/j.cub.2017.05.084.
81. Galtieri, D.J., Estep, C.M., Wokosin, D.L., Traynelis, S., and Surmeier, D.J. (2017). Pedunculopontine glutamatergic neurons control spike patterning in substantia nigra dopaminergic neurons. eLife *6*, e30352. https://doi.org/10.7554/eLife.30352.
82. Futami, T., Takakusaki, K., and Kitai, S.T. (1995). Glutamatergic and cholinergic inputs from the pedunculopontine tegmental nucleus to dopamine neurons in the substantia nigra pars compacta. Neuroscience Research *21*, 331–342. https://doi.org/10.1016/0168-0102(94)00869-H.
83. Good, C.H., and Lupica, C.R. (2009). Properties of distinct ventral tegmental area synapses activated via pedunculopontine or ventral tegmental area stimulation in vitro. J Physiol *587*, 1233–1247. https://doi.org/10.1113/jphysiol.2008.164194.
84. Evans, R.C., Twedell, E.L., Zhu, M., Ascencio, J., Zhang, R., and Khaliq, Z.M. (2020). Functional Dissection of Basal Ganglia Inhibitory Inputs onto Substantia Nigra Dopaminergic Neurons. Cell Reports *32*, 108156. https://doi.org/10.1016/j.celrep.2020.108156.